Pre-eruptive reservoir conditions of the peralkaline Rungwe Pumice (Tanzania) Plinian eruption from haüyne-hosted melt inclusions

Lorenzo Cappelli - *Department of Geosciences, Environment and Society; Université libre de Bruxelles; Bruxelles, 1050, Belgium.* lorenzo.cappelli@ulb.be

Paul A. Wallace – *Department of Geosciences, Environment and Society; Université libre de Bruxelles; Bruxelles, 1050, Belgium.*

Department of Earth and Environmental Sciences; Ludwig-Maximilians-Universität München; München, 80539, Germany. Paul.Wallace@min.uni-muenchen.de

Gerald G.J. Ernst – no affiliation. plumeman2000@yahoo.co.uk

Evelyne Mbede – *School of Mines and Geosciences; University of Dar es Salaam; Dar es Salaam, 35052, Tanzania.* embede@gmail.com

Shimba Kwelwa – *AngloGold Ashanti; Geita, 532, Tanzania.* skwelwa750@gmail.com

Edista Abdallah – *School of Mines and Geosciences; University of Dar es Salaam; Dar es Salaam, 35052, Tanzania.* edisteralex@gmail.com

Karen Fontijn – *Department of Geosciences, Environment and Society; Université libre de Bruxelles; Bruxelles, 1050, Belgium.* karen.fontijn@ulb.be

Keywords: East African Rift; Melt Inclusions; Peralkaline magmas; Plinian-style eruptions; Storage conditions.

ABSTRACT

The style and explosivity of volcanic eruptions are primarily governed by the interplay between conduit dynamics (e.g., magma ascent rate and degassing efficiency) and pre-eruptive magmatic conditions, both of which influence magma rheology. In highly alkaline magmas (i.e., agpaitic index > 1), the depolymerising effect of alkaline elements lowers melt viscosity at a given temperature, theoretically favouring less explosive eruptions—even in silica-rich systems. However, several well-documented eruptions demonstrate that silica-undersaturated peralkaline magmas (e.g., trachytes and phonolites) can produce highly explosive Plinian events, suggesting that additional factors control eruption style. In the East African Rift, volcanoes with peralkaline compositions have exhibited both explosive and effusive behaviour. To better understand the controls on explosivity, we investigated the pre-eruptive magmatic system of the Plinian eruption that produced the Rungwe Pumice (RP) deposit in southern Tanzania. The late-stage evolution of the plumbing system was reconstructed through haüyne-hosted melt inclusions (MIs), revealing that an evolved magma body was stored at relatively shallow depths shortly before the eruption. Water concentrations in MIs, measured via transmitted Fourier-transform infrared spectroscopy, indicate relatively water-poor conditions (~4.8 wt.%) and shallow water saturation depths (~3.5 km). Our findings suggest that volatile concentration alone does not fully explain the explosive behaviour; rather, the degree of water undersaturation and conduit dynamics must also be considered as key factors influencing eruption style.

1 INTRODUCTION

The eruptive behaviour of magma is governed by the exsolution of volatiles and the efficiency of gas-melt decoupling during ascent in the volcanic conduit (e.g., Gonnermann and Manga, 2007; Cassidy et al., 2018). These processes are strongly controlled by several factors, including ascent—and thus decompression—rate, conduit geometry, magma permeability, and the presence of crystals acting as bubble nucleation sites (e.g., Gonnermann, 2015; Shea, 2017). However, a crucial role is played by melt composition—particularly major element and dissolved volatile concentrations—which, along with reservoir temperature, pressure, and volatile saturation, directly impacts melt rheology (Sparks, 1978; Dingwell, 1996; Giordano et al., 2008; Degruyter et al., 2012; Gonnermann, 2015 and references therein). A primary control on explosivity is therefore played by water, the most abundant volatile phase dissolved in melts, as it drives decompression-induced supersaturation, bubble nucleation and growth, and ultimately, magma foaming (Gonnermann and Manga, 2007). At the same time, rheology dictates how magma responds to strain and accommodates stress, ultimately influencing whether it undergoes brittle failure and fragmentation (Dingwell and Webb, 1989; Dingwell, 1996; Cassidy et al., 2018).

The viscous rheology of polymerised, high-silica, calc-alkaline melts, combined with elevated water contents, often leads to violent Plinian-style eruptions (e.g., Walker, 1981; Cioni et al., 2015). In contrast, higher alkali (Na and K) concentrations depolymerise the Si-O bonds in phonolitic or peralkaline trachytic and rhyolitic melts resulting in significantly lower melt viscosities—up to two orders of magnitude lower for rhyolite under equivalent temperature and water content conditions—compared to their calc-alkaline counterparts (Giordano et al., 2008; Di Genova et al., 2013). Lower viscosities generally facilitate efficient outgassing and prolonged resistance to strain, potentially resulting in weaker eruptive explosivity. However, several well-documented cases demonstrate that highly energetic, Plinian-style eruptions can also originate from such lower-viscosity, alkali-rich magmas (e.g., Mahood, 1984; Cioni et al., 1999; White et al., 2012), even under water-undersaturated reservoir conditions (Andújar and Scaillet, 2012a). While high-alkaline series magmas are less abundant on Earth than the calc-alkaline series, which dominate continental arc settings (e.g., Stern, 2002 and references therein), they occur across all geological environments, from subduction zones to intraplate hotspots, and are particularly common in continental rift settings (e.g., Mahood, 1984; Avanzinelli et al., 2004; Andújar and Scaillet, 2012b; Esposito et al., 2018; Jeffery and Gertisser, 2018), especially along the East African Rift (EAR; e.g., Leat, 1984a; Macdonald and Scaillet, 2006; White et al., 2012; Fontijn et al., 2013; Hutchison et al., 2016; Tadesse et al., 2019; Wallace et al., 2025).

Volcanism within the EAR is characterised by extensive, multicentred volcanic systems whose Quaternary activity includes Plinian-style eruptions, sometimes culminating in caldera collapses (e.g., Williams et al., 1984; Macdonald, 1987; Fontijn et al., 2018). Magmatic products range from silica-undersaturated to silica-saturated compositions but are generally enriched in alkali elements. The limited documentation of many of these volcanic centres results in a significant underestimation of volcanic hazards in densely populated regions across the EAR (Biggs et al., 2021).

To better understand the factors controlling the explosivity of moderate-viscosity, peralkaline systems widespread along the EAR, we investigated the pre-eruptive conditions of the ~4 ka Rungwe Pumice (RP) eruption. These parameters are critical indicators of the current state of magmatic reservoirs and the potential for future unrest. The RP deposit originates from a Plinian-style eruption of Rungwe volcano in the Rungwe Volcanic Province (RVP; Tanzania; (Fontijn et al., 2011). Relevant insights into pre-eruptive physical and chemical conditions and processes are preserved in crystal-hosted melt inclusions (MIs). These melt pockets, trapped in crystal imperfections during growth, can maintain chemical equilibrium with the original melt and remain largely unaffected by its subsequent evolution during ascent (e.g., Esposito et al., 2014). Particularly, while the pumice matrix melt undergoes extensive degassing during ascent, MIs can retain the original volatile concentrations (e.g., Cioni, 2000; Esposito et al., 2014; Cannatelli et al., 2016; Steele-MacInnis et al., 2017). In this study, the storage conditions, melt chemistry and water content within the pre-eruptive reservoir are analysed using MIs hosted in haüyne crystals (feldspathoid of the sodalite group) collected from different stratigraphic horizons of a type section of the RP deposit (i.e., KF176).

2 GEOLOGICAL CONTEXT

The EAR is the largest active divergent continental margin and is originated by the divergence of the Somalian and Nubian (African) Plates. It extends over 3000 km from the Afar triple junction to Mozambique (Saria et al., 2014). In its central section, the rift encounters the thick and rigid Tanzanian craton, splitting into the Western and Eastern branches (Saria et al., 2014; Ebinger et al., 2017).

Volcanism occurs throughout the EAR but is predominantly concentrated along the more mature Eastern branch (**Fig. 1a**). However, some of the most active present-day volcanic centres are located along the Western branch, which hosts four of the twenty-one EAR volcanoes known to have erupted in historical times (Wadge et al., 2016). Eruptive activity across the EAR varies from effusive fissure eruptions to caldera-forming Plinian-style events (Macdonald, 1987; Fontijn et al., 2011, 2018). Magmatic products range from mafic to silicic compositions, typically following alkaline or peralkaline series, with their petrogenesis extensively studied (e.g., Macdonald and Scaillet, 2006; Hutchison et al., 2018).

The Rungwe Volcanic Province (RVP) spans over 1500 km^2 and is located in the Western branch of the EAR, south of the Tanzanian Craton at the junction of the NW-SE trending Tanganyika-Rukwa rift, the N-S trending North Malawi rift and the NE-SW trending Usangu basin (**Fig. 1a;** Ebinger et al., 1993). The RVP comprises three main Holocene volcanic centres—Rungwe, Ngozi and Kyejo—surrounded by hundreds of smaller eruptive centres, which are scattered throughout the province along two dominant NW-SE and NE-SW structural alignments (Fontijn et al., 2010a).

Volcanism in the RVP began approximately 9 Ma, with an initial phase (lasted until the Early Pleistocene) characterised by alternating effusive and explosive eruptions of alkaline magmas from volcanic centres that are now buried or eroded (Fontijn et al., 2012 and references therein). The most recent phase of activity began with basaltic and trachytic lava flows spreading northward into the Rukwa Rift and Usangu Basin, eventually focusing within a ~30 km-wide NW-SE trending sector encompassing the three main volcanic centres and their satellite cones. This phase transitioned into a predominantly explosive stage, producing large eruptions such as the 10–12 ka Kitulo Pumice eruption and the <1 ka Ngozi Tuff eruption, which formed the present-day Ngozi caldera depression (Fontijn et al., 2010b). In contrast, Kyejo's edifice developed through mildly explosive and effusive activity from smaller centres (Harkin, 1960; Fontijn et al., 2010a), culminating in the RVP’s only recorded historical eruption, the 1800 CE Sarabwe lava flows (Fontijn et al., 2012).

Rungwe is the largest volcanic edifice in the RVP and is centrally located within the province (**Fig. 1b**). It is a young (0.25 ±0.01 Ma, whole-rock K-Ar age; Ebinger et al., 1989), stratovolcano composed of basaltic, phonolitic, and trachytic lava flows. Its summit was truncated by a sector collapse unrelated to magmatic activity (Fontijn et al., 2012), later infilled by multiple silicic domes and tephra cones. The most prominent deposit associated with the whole RVP is the ~4 ka Rungwe Pumice (RP) deposit (Fontijn et al., 2010b, 2011). More recent eruptions include the Isongole Pumice—Rungwe’s second-most explosive event (VEI 4; Newhall and Self, 1982)—and three weaker explosive eruptions dated to <1.5 ka (i.e., Ngumbulu Tephra; Aphyric Pumice, Kizungu Tephra; Fontijn et al., 2010b). Overall, Rungwe has experienced at least one explosive eruption every 500 years, with activity ranging from violent Strombolian to Plinian events (Fontijn et al., 2010b).

2.1 Rungwe Pumice eruption

The RP deposit consists of a massive pumice lapilli fall deposit that blankets the entire RVP. Radiocarbon dating and sedimentary records from Lake Masoko place the eruption at approximately 4 ka (Garcin et al., 2006; Fontijn et al., 2010b). The deposit is lithic-poor and predominantly composed of cream-coloured pumice lapilli of high-alkaline, trachytic composition (whole-rock; Fontijn et al., 2013). A minor fraction (<1wt%) of grey/banded pumice has been identified, interpreted as evidence of magma mingling with a slightly more mafic melt (Fontijn et al., 2011). The RP deposit storage conditions were inferred using the titanomagnetite-ilmenite pair geothermometer (Ghiorso and Evans, 2008) which indicated a temperature of 925 °C and an oxygen fugacity in the NNO+0.25-NNO+0.45 range (nickel-nickel oxide buffer; Fontijn et al., 2013). Reservoir ponding depths were estimated at 2.5-13 km within the shallow-mid crust with the clinopyroxene-liquid barometer (Putirka, 2008; Fontijn et al., 2013). A maximum pre-eruptive water content of 5.5 wt.% (Fontijn et al., 2013) was estimated using the by-difference method on melt inclusion compositions (Devine et al., 1995).

RP's pumice ground mass is microlite-free, phenocrysts poor (<5 vol.%; Fontijn et al., 2013) and highly vesicular (Fontijn et al., 2013; Cappelli et al., 2025). Alkali feldspar is the dominant free mineralogical component, with subordinate biotite, clinopyroxene and Fe-Ti oxides. Plagioclase, though rare, is exclusively present in grey-banded pumices (Fontijn et al., 2013). Notably, cyan-coloured haüyne occurs in the RP deposit, distinguishing it from most other RVP deposits and serving as a field marker for identifying RP outcrops (Fontijn et al., 2011).

More than 100 RP outcrops were mapped across the province extending up to 28 km from Rungwe summit, where the deposit maintains a thickness of 30 cm. A ~1 m-thick tephra layer attributed to the RP eruption was found in Lake Masoko's sedimentary record around 25 km SSE of Rungwe (Garcin et al., 2006; Fontijn et al., 2012). While no clear evidence of more distal deposits remains—likely due to pedogenesis—sediment cores from Lake Malawi, ~115 km SE of Rungwe, contain ash horizons chronologically linked to the RP eruption (Fontijn et al., 2011).

RP outcrops are radially distributed around the summit, with near-circular isopleths indicating that the eruption originated from the present-day Rungwe summit and likely occurred under wind-still conditions (Fontijn et al., 2011). The maximum lithics method (Carey and Sparks, 1986) suggests an eruptive column height of 30-35 km (Fontijn et al., 2011), which was likely sustained throughout the entire duration of the eruption, as no associated large pyroclastic density current deposits have been identified. The peak mass discharge rate, estimated from a range of inferred column heights, falls between 2.8 and 4.8 $\times 10^8$ $kg \cdot s^{-1}$, while the minimum erupted volume is approximately 1.4 km^3 dense rock equivalent (Fontijn et al., 2011). Based on these parameters, the RP eruption is classified as Plinian, with a Volcanic Explosivity Index of 5 (Newhall and Self, 1982; Fontijn et al., 2011).

A reference section for the RP deposit, designated as KF176 in previous studies (Fontijn et al., 2010b, 2011, 2013), was identified approximately 11.7 km SSE of the Rungwe summit. This ~2.5 m-thick, massive pumice deposit exhibits an unimodal, well-sorted grain-size distribution (sorting $\sigma_\varphi < 2$) centred around the median at -2.2 φ (~4.5 mm)—except for the finer and reversely graded base (lower 50 cm; Fontijn et al., 2011)—and is bounded by overlying and underlying palaeosols. The deposit was previously sampled through its entire thickness by Fontijn et al. (2011) and subdivided into 14 subsamples at 20-25 cm intervals from base to top, sequentially labelled KF176-B to KF176-O, with KF176-A corresponding to the basal palaeosol.

3 METHODS

3.1 Componentry analyses

The different types of components constituting the RP deposit were investigated by counting 3000 particles within the medium (0.35-0.50 mm) and coarse (0.71-1.00 mm) ash fractions for each subsample of the type section (KF176-B to KF176-O). With the aid of a stereomicroscope, the particles were characterised and classified into three categories: juvenile (pumice), lithics and crystals. Detailed methodology and results are provided in **Supplementary Information**.

3.2 FTIR analysis

The total H_2O and CO_2 content dissolved in MI glasses was quantified using transmission Fourier Transform Infrared (FTIR) spectroscopy, by applying the Beer-Lambert Law (§3.5). FTIR spectroscopy measures the absorbance of specific wavelengths in the near-/mid-infrared range caused by the vibrational modes of the target analytes (e.g., von Aulock et al., 2014). A detailed description of the methodology and parameters used is provided in the **Supplementary Information**.

FTIR spectra were acquired at the ISTO-CNRS laboratory (Orleans, France) using a Nicolet 6700 FTIR spectrometer connected to a Nicolet Continuμm Infrared Microscope equipped with an MCT IR Detector Module. The acquiring setup consisted of a Globar light source, an XT-KBr beamsplitter and a 32x infinity-corrected Schwarzschild objective matching to a 32x condenser. The square beam aperture was set at 20x20 μm or 40x40 μm for larger MIs, while a 15x15 μm aperture was exceptionally used for the smallest MIs. Water concentration was determined from the fundamental stretching vibration of O-H bonds at 3550 cm^{-1}, which retains a strong signal-to-noise ratio. However, at higher water concentrations, this peak can become saturated unless the sample is extremely thin (von Aulock et al., 2014). In such cases, water content was estimated using the combined absorbance bands of hydroxyl groups (OH^-; 4500 cm^{-1}) and molecular water (5200 cm^{-1}). Molecular CO_2 yields a vibrational peak at 2351 cm^{-1} (Brooker et al., 1999), while dissolved carbonate species (CO_3^{2-}) produce an absorption doublet between 1670 and 1375 cm^{-1} (Brooker et al., 1999). Spectra were therefore acquired over a wavenumber range of 1200-6000 cm^{-1} with a spectral resolution of 4 cm^{-1} (**Fig. 2**).

MIs and embayments (i.e., inclusions open on one side) are hosted in various RP crystalline phases, including alkali feldspars (as tiny lamellar inclusions), pyroxenes, and Fe-Ti oxides (hardly detectable). However, haüyne-hosted MIs were the most suitable for investigation due to their abundance, well-developed morphology, and larger sizes. Additionally, haüyne—the Ca endmember of the haüyne-nosean series ($[Na_{5\text{-}8}K_{0\text{-}1}Ca_{0\text{-}2}(Fe,Mg)_{0\text{-}1}]_8[Al_6Si_6O_{24}]\cdot(SO_4,S,Cl,OH,CO_3)_{1\text{-}2}\cdot nH_2O\cdot mCO_2$)—reportedly forms late in the crystallisation sequence (e.g., Harms and Schmincke, 2000). Notably, RP haüyne never occurs as a mineral inclusion, but instead hosts inclusions of apatite, ilmenite and biotite (Fontijn et al., 2013), suggesting it could entrap a melt representative of the late pre-eruptive conditions.

Four stratigraphic subsamples representing different horizons of the type section were selected: bottom (KF176-C), middle (KF176-G and KF176-K), and top (KF176-O). More than 100 haüyne crystals (0.5–2 mm in size) were handpicked from manually crushed pumice clasts. Crystals were carefully examined to identify potential melt inclusion assemblages (MIAs; Bodnar and Student, 2006; Esposito et al., 2014) and to discard unsuitable MIs (e.g., inclusions smaller than 15 μm, or those with excessive bubbles obstructing the FTIR beam path). Suitable crystals were embedded in a thermosetting resin (Crystalbond™ 509) and doubly polished (von Aulock et al., 2014) with diamond pastes to expose MIs on two opposed sides, producing thin crystal wafers (tens of micrometres thick). Due to variations in crystal availability and MI suitability, the final dataset included a variable number of MIs per horizon, for a total of 86 MIs and embayments.

For FTIR analysis, crystals were gently removed from the resin by heating on a hot plate, rinsed in acetone to remove resin residuals, and placed over a CaF_2 window. A background spectrum on the CaF_2 window was collected for calibration before each measurement, and whenever environmental conditions (e.g., temperature, CO_2 concentration, humidity) affected spectral trends. Absorbance values were determined using peak heights rather than peak areas to minimize distortion effects, and a linear baseline was adopted. A minimum of three scans per MI were collected to ensure reproducibility, spectra were then averaged using Omnic™ software data processing tools to reduce the spectral noise. FTIR spectra were acquired at both the MI centre and closer to rims to evaluate water content consistency, while embayments were scanned in their most internal portions.

Since haüyne can host both structural and molecular volatile phases, the same FTIR procedure used for MIs was applied to estimate the H_2O and CO_2 concentrations in MI-hosting haüyne crystals. Haüyne is an isotropic crystal with a cubic symmetry, meaning its absorbance is unaffected by the orientation of optical indicatrix axes, allowing analysis in random orientations (e.g., Bellatreccia et al., 2009). Spectra were acquired close to the MIs adopting the same acquisition settings and a beam aperture of 40x40 μm. Haüyne's water absorbance spectrum consists of three overlapping overtones in the ~2800–3700 cm^{-1} range, therefore the integrated absorbance was used (Bellatreccia et al., 2009), while the stretching of CO_2 molecules gives a well-defined absorbance peak at ~2350 cm^{-1} (**Fig. 2**; Bellatreccia et al., 2009).

3.3 EPMA analysis

Major element concentrations of MI previously analysed with FTIR were measured with a JEOL JX-iHP200F field emission electron probe micro-analyser (EPMA) at the IMAP laboratories of the Université Grenoble-Alpes (France). The crystal wafers were embedded in epoxy resin, polished with diamond pastes (down to 1 µm diamond grade), and carbon coated. Analyses were conducted at an acceleration voltage of 15 kV, a probe current of 5 nA, and a defocused beam diameter of 15 µm. The analytes were measured with five wavelength dispersive spectroscopy (WDS) spectrometers and one energy dispersive spectroscopy (EDS) spectrometer (Si only, with StHs6-80 glass as calibration material). Sodium was analysed first to avoid element dispersion and a ZAF correction was applied. The StHs6-80, Atho-G and KE12 reference materials (Jochum et al., 2006) were analysed three times every 30-40 measurements to evaluate accuracy. Each MI was measured at least three times for consistency. Simultaneously, major element concentrations of MI-hosting haüyne crystals were analysed under the same conditions, using Cr-Augite, Ortho-Bl3, and Ortho-Bl2 as secondary standards.

Groundmass glass chemistry of pumices was also analysed using EPMA. Pumiceous glass shards were obtained from the 125–250 µm grain-size fraction of manually crushed pumice clasts from the four stratigraphic subsamples investigated. The crushed material was wet sieved at 80 µm in demineralised water to remove accretionary dust or clays, then embedded in epoxy resin, ground and polished with diamond pastes down to 1 µm grade. The same instrument and analytical conditions used for MI analyses were applied, with a 2 nA probe current and a 5 µm beam diameter. Glass chemistry of each subsample was analysed at least eight times for reproducibility on different glass shards.

Additionally, major element concentrations in alkali feldspar were analysed along core-to-rim transects consisting of five measurement points to assess chemical variations during crystallisation. Crystals were handpicked from the 0.5–2 mm grain-size fraction of crushed pumices, embedded in epoxy resin, and polished following the same preparation steps as other samples. Cr-Augite, Ortho-Bl3, and Ortho-Bl2 were used as secondary standards.

3.4 Bulk rock analysis

Whole-rock major and trace element concentrations were determined for pumices of each deposit subsample (KF176-B to KF176-O) at the Laboratoire G-Time of the Université libre de Bruxelles (Belgium). Samples were manually crushed to a fine powder in an agate mortar and prepared as a solution by alkaline fusion. Loss on ignition was estimated by heating the powders at 800 °C for 2h after drying them completely at 105 °C for over 24h. Major elements were measured with a Thermo Fisher Scientific iCAP inductively coupled plasma-optical emission spectrometer (ICP-OES) using Y as an internal standard. Trace elements were analysed with an Agilent 7700 quadrupole inductive-coupled plasma mass spectrometry (Q-ICP-MS) operated with a He-filled collision cell. The USGS standards BHVO-2, RGM-2, and QLO-2 were analysed as reference materials and one sample duplicate was measured for reproducibility. The total reproducibility based on reference materials was estimated to be better than 4% and 12% relative standard deviation for major and trace elements respectively.

3.5 Volatile concentrations

The relationship between infrared light absorption and analyte concentration in a sample follows the Beer-Lambert Law (Stolper, 1982), which requires knowledge of thickness, density and molar absorptivity index of the analysed phase. A detailed description of the methodology and parameters is provided in **Supplementary Information**.

To minimize uncertainty introduced by operator bias (e.g., optical focus recognition), MI and host crystal thicknesses were determined using two independent methods and compared. First, a flat-anvil digital micrometre (resolution = 1 µm; accuracy = ±2 µm) was used, which reduces the risk of damaging the fragile crystals compared to a pointed micrometre. Then, the thickness was measured using a LEITZ DMR optical microscope equipped with a calibrated and automated focus stage (resolution = 2 µm). Each measurement was repeated two or three times per crystal.

For MI glass, an average density of 2.25 ±0.01 g·cm^{-3} was estimated as a function of its chemical composition (Lange, 1997) which requires glass volume determination. Volume was estimated using the temperature-dependent equations for hydrated iron-bearing silicate glasses (Lange and Carmichael, 1987; Ochs III and Lange, 1999; Richet et al., 2000), with temperature estimated using an alkali feldspar-liquid geothermometer (Eq. (24b) in Putirka, 2008). To assess equilibrium between feldspar rims and pumice groundmass, petrographic observations of thin sections of lapilli-sized clasts from five stratigraphic subsamples (KF176B; KF176E; KF176H; KF176K; KF176N) were conducted using optical petrographic microscopy and scanning electron microscopy (SEM). SEM imaging was performed in backscattered electron mode, at 15 kV using a Hirox SH5500P equipped with a Bruker EDS Quantax detector at the Laboratoire G-Time of the Université libre de Bruxelles (Belgium). No disequilibrium features were identified. However, before applying feldspar-based thermometry, textures of feldspars analysed with EPMA were carefully inspected also with SEM. Haüyne density was assumed to be 2.4 g·cm^{-3} (Taylor, 1967).

A molar absorptivity index of 66.9 ±5.8 L·mol^{-1}·cm^{-1} (Behrens and Hahn, 2009), experimentally determined for high-alkali trachytic glasses, was used for the 3550 cm^{-1} overtone of MI absorbance spectra. Indices for the 4500 cm^{-1} and 5200 cm^{-1} overtones were estimated through multiple linear regression (Di Matteo et al., 2004), with the water content calculated from the 3550 cm^{-1} band as a fixed term. The resulting molar absorptivity indices, with 90% confidence bounds as subscripts and superscripts, were $1.35_{1.01}^{1.71}$ and $1.03_{0.69}^{1.38}$ L·mol^{-1}·cm^{-1} for the 4500 cm^{-1} and 5200 cm^{-1} overtones, respectively. These values are similar but slightly different from those previously estimated for trachytic (1.58 and 1.36 L·mol^{-1}·cm^{-1} respectively; Di Matteo et al., 2004) and phonolitic (1.25 and 1.10 L·mol^{-1}·cm^{-1} respectively; Carroll and Blank, 1997) glass. Integrated molar absorptivity indices for H_2O and CO_2 in haüyne were fixed at 5422 and 1866 L·mol^{-1}·cm^{-2} respectively from haüynes of similar compositions (Bellatreccia et al., 2009).

4 RESULTS

4.1 Componentry analyses

Cream-white, highly vesicular pumice dominates each horizon of the deposit in both the medium (46-81% of the components) and coarse (67-90%) ash fractions but gradually decreases toward the top of the stratigraphic sequence mirroring an opposite increase in crystals content (up to 45 %; **Fig. 3**). Lithics fragments are a minor but consistent component (~6%) throughout the sequence, except for a peak in the basal 40 cm (**Fig. 3**). Pumice morphologies are predominantly solid, subrounded, and equidimensional, with a small portion (~5%) of tube pumice. Free crystal phases primarily consist of alkali feldspar (84-99% of the total crystal content), accompanied by subordinate biotite, Fe-Ti oxides, haüyne, pyroxene, and titanite, with accessory olivine (**Supplementary Information**). Relative crystal abundances remain nearly constant throughout the sequence, except for haüyne, which progressively increases from bottom to top, never exceeding 3% of the total crystal population (**Supplementary Information**).

4.2 MI textures

A comprehensive list and description of the haüyne-hosted MIs investigated are provided in **Supplementary Table 1**. Pale to dark brown MIs are ubiquitous within haüyne crystals of the RP deposit. Their volumes span approximately five orders of magnitude (10^3-10^7 μm^3; equivalent ellipsoid volume) and sum together can occupy a significant portion of their host crystals.

The vast majority of MIs exhibit blunted, ellipsoidal to sub-spherical morphologies (**Fig. 4a**), though mushroom-shaped inclusions are also common. These often occur in coaxial pairs connected either to each other or to the crystal exteriors (embayments) through a tapered bottleneck (**Fig. 4b, c**). In contrast, sub-planar (**Fig. 4d**) and fully faceted MIs are rare, with the latter accounting for only ~2% of the inclusions investigated. Most embayments display irregular (*complex* as in Ruefer et al., 2021), sub-cylindrical (*simple*), or bulbous morphologies. MIs of different sizes and shapes can coexist within the same haüyne crystal, but their spatial distribution appears arbitrary, making the recognition of MIAs challenging.

Crystalline phases are absent within MIs, while the number and size of bubbles were the key distinguishing features for MI selection in analyses. MIs can be free of bubbles (**Fig. 4a**), host a single spherical bubble (**Fig. 4a**), or be partially to entirely filled with a multitude of microscopic bubbles (termed microvesicular MIs; **Fig. 4c**). Only bubble-free and single-bubble inclusions which do not show any evidence of post-entrapment modification (e.g., leaking through fractures) were considered for further analyses. Bubble-free MIs are the most abundant overall, especially at the lower stratigraphic levels, followed by single-bubble MIs and microvesicular MIs. In rare cases, MIs contain multiple bubbles (usually fewer than 10) of widely variable size (**Fig. 4e**). Notably, MIs hosted within the same crystal exhibit generally the same bubble contents.

The size of single bubbles scales with the volume of their host MIs (**Fig. 4g**), occupying on average 2.39 ±1.80 vol.% of the inclusion. In contrast, individual microscopic bubbles within microvesicular clusters contribute at most 0.23 vol.% (0.04 ±0.06 vol.% on average; **Fig. 4h**). The large standard deviation arises from the assumption of an equivalent ellipsoidal volume for MI volume estimation. For multiple-bubble MIs, a total bubble volume is calculated as the sum of all individual bubbles within the same MI—an approach that resulted unfeasible for microvesicular MIs. The total bubble volume in multiple-bubble MIs scales similarly to that of single-bubble MIs (**Fig. 4g**), resulting in comparable volume occupancies (**Fig. 4h**).

Embayments frequently contain multiple large bubbles (10.77 ±0.78 vol.% on average) that tend to concentrate near the outlet where they adopt ellipsoidal to droplet-like shapes (**Fig. 4f**).

4.3 Glass geochemistry

Melt inclusions have a homogeneous trachytic-phonolitic composition, containing ~61 ±0.3 wt.% SiO_2 and elevated alkaline elements concentrations (**Fig. 5**). The agpaitic index ([Na+K]/[Al]) ranges between 0.99 and 1.07 with an average at 1.02 ±0.02 while the Mg# ([Mg]/[Mg+Fe]) is 0.22 ±0.01 on average. The full range of sample and reference material chemical compositions is provided in **Supplementary Table 2**. Elemental comparisons reveal no evident trends, except for a positive correlation between CaO and MgO and a negative correlation between Na_2O and K_2O (**Fig. 6**). Embayments and MIs share similar major element compositions, with the exception of slightly higher K_2O concentrations in MIs. Within individual MIs or embayments, major element compositions remain chemically homogeneous, showing no systematic variation from core to rim (e.g., relative standard deviations of 0.36 ± 0.20% for SiO_2 and 1.34 ± 1.09% for Na_2O), even for mobile elements like Cl and S in open embayments. Major element concentrations in MIs remain largely consistent across stratigraphic horizons (i.e., relative standard deviation range from 0.16% in FeO to 9.42% in P_2O_5), though a slight increase of K_2O and TiO_2, and a decrease in Na_2O are observed from base to top of the sequence (**Fig. 7**). The chemical composition of pumice groundmass glass closely resembles that of MIs in terms of silica and most major elements (**Fig. 6**), but it is slightly depleted in K_2O (-7.0 ±1.0% on average) and enriched in Na_2O (+9.4 ±4.4% on average) (**Fig. 6**). In contrast, tephra glass exhibits a more systematic variation in oxide concentrations from the base to the top of the stratigraphic sequence, with K_2O, MgO, TiO_2, SO_3, and CaO decreasing and Na_2O and Cl increasing (**Table 1; Fig. 7**).

Water concentrations in MIs, determined via FTIR absorption, range from 2.29 wt.% to 5.88 wt.%, with an average of 3.63 ±0.78 wt.% (**Fig. 8**). No significant difference is observed between MIs with or without a gas bubble (3.75 ±0.75 wt.% and 3.63 ±0.89 wt.% respectively), or across the stratigraphic sequence. In contrast, embayments contain slightly less water, with an average of 3.14 ±1.17 wt.%. The uncertainty derived from the error propagation of all parameters in the Beer-Lambert equation is on average 12 ±4%, which aligns with the typical uncertainty range for such estimations (e.g., 10-20%; Agrinier and Jendrzejewski, 2000; Wysoczanski and Tani, 2006; von Aulock et al., 2014). Among the sources of error, thickness uncertainty is a major contributor, with a ±1 μm variation yielding an average ~3% error in water content estimation, equivalent to 0.1 wt.% H_2O.

FTIR spectra reveal no absorbance peak at 2351 cm^{-1} for the molecular CO_2 overtone (Brooker et al., 1999), even in the thickest MIs, indicating that molecular CO_2 in the glass is likely below the thickness-dependent detection limit, ranging from tens up to a hundred ppm (von Aulock et al., 2014; Rose-Koga et al., 2021). In lower-silica and depolymerised melts, dissolved carbonate species (CO_3^{2-}) dominate over molecular CO_2 in C-O species speciation (Brooker et al., 1999; Morizet et al., 2013); however, most of our spectra exhibit significant noise below 1600-1550 cm^{-1}. Even in spectra with a high signal-to-noise ratio, no evident carbonate doublet is observed, which may be masked by the H_2O_{mol} peak at 1650 cm^{-1}. As a result, dissolved CO_2 concentrations cannot be quantified for MIs, even in bubble-free inclusions, suggesting a generally limited CO_2 uptake in bubbles.

4.4 Crystals geochemistry

4.4.1 Haüyne

Haüyne crystals are chemically homogenous, exhibiting no evident zonation even under scrupulous SEM investigation. Crystals from different horizons share similar chemical compositions (**Supplementary Table 2**), with the exception of a subtle, progressive increase in SO_3 (wt.%) from the base to the top of the sequence. Water content within haüyne, estimated via FTIR analyses, is on average of 1.53 ±0.52 wt.%, while CO_2 concentrations range from 0.02 wt.% to 0.33 wt.%. The stoichiometric formula of haüyne crystals can be expressed as:

$$(Na_{5.44-6.15}Ca_{1.61-1.87}K_{0.2-0.26}Fe_{0.04-0.05}Mg_{0.01-0.03})_{\Sigma\cong 8}(Al_{5.78-5.86}Si_{6.14-6.22}O_{24})\cdot \\ \cdot[(SO_4^{2-})_{1.37-1.73}(Cl^-)_{0.07-0.14}(OH^-)_{0.18-0.50}]_{\Sigma=2}\cdot nH_2O\cdot mCO_2$$

where *n* ranges from 0.51 to 2.68 and *m* from 0.01 to 0.46. The unit formula was normalised assuming (Si + Al) = 12, while the anionic site sum was set to 2 to account for water occupancy. Since the overtone at ~3500 cm^{-1} in FTIR spectra, used for water estimation, does not resolve water speciation, all OH^- was assigned to the anionic site to complete a valence of 2 (Bellatreccia et al., 2009), with any remaining water included as molecular H_2O. Sulphur was entirely allocated to sulphate (SO_4^{2-}) consistent with haüyne's stability under oxidising conditions (Baudouin and Parat, 2015 and references therein) and the presence of sharp overtones at ~2200 cm^{-1} in FTIR spectra (Bellatreccia et al., 2009). The consistent presence of Ca in the stoichiometric formula confirms that all analysed crystals are compositionally closer to the haüyne end-member in the haüyne-nosean solid solution. However, a progressive increase in Ca and SO_4, coupled with a decrease in Na, is observed across the stratigraphic sequence from bottom to top, indicating subtle variations along the haüyne-nosean series. Crystal edges are commonly altered to unidentified zeolitic phases enriched in Si and Al, often banded with Ca enrichments (**Supplementary Fig. 3**).

4.4.2 Alkali feldspars

The composition of alkali feldspars ranges from $Ab_{71}Or_{28}An_1$ to $Ab_{54}Or_{44}An_2$ (**Supplementary Fig. 4a**; **Supplementary Table 2**). Textural observations do not reveal any visible chemical zonation within the crystals (**Supplementary Fig. 4a, b**). Across the stratigraphic section, the anorthite component progressively increases from base to top. Such a trend corresponds to a gradual increase in CaO at the expense of Na_2O, while K_2O remains essentially stable.

4.5 Bulk rock geochemistry

The bulk composition of pumice closely resembles that of the groundmass glass in terms of major elements (**Fig. 5**) but is slightly depleted in SiO_2 (-3.6 ± 0.9 wt.% on average) and Na_2O (-2.3 ±0.5 wt.% on average), while being enriched in Al_2O_3 (+1.6 ±0.5 on average). The significant depletion of alkali in bulk pumices may be partially attributed to weathering, as RP material exhibits noticeable alteration in hand specimens. Across the stratigraphic sequence, SiO_2 content progressively decreases, whereas TiO_2, CaO, MgO, and P_2O_5 concentrations increase from base to top. The other oxides remain relatively stable. Notably, the composition of the basal horizon B differs significantly from the overlying horizons, displaying anomalous trends in Al_2O_3, FeO_{tot}, MnO, K_2O and TiO_2 (**Fig. 5**).

Trace element concentrations of bulk pumice are reported in **Table 1**. The primitive mantle-normalised (McDonough and Sun, 1995) concentrations are generally higher than those reported for Rungwe basalts (Castillo et al., 2014) but exhibit similar overall trends (**Fig. 9a**). The highest normalised values are observed for highly incompatible U and Th. REE concentrations, normalised to the primitive mantle (McDonough and Sun, 1995), indicate higher LREE concentrations relative to HREE, along with a pronounced negative Eu anomaly (**Fig. 9b**). Across the stratigraphy, progressive increasing or decreasing trends are evident (**Fig. 9c**). Specifically, from base to top, most middle REE and LILE (except Rb) tend to increase, while extreme HREE, LREE and HFSE show opposite trends. Fe-Mg substituent metals do not exhibit any clear trend. Notably, several elements in the basal horizon (i.e., sample KF176-B) display anomalous values compared to the rest of the sequence (**Fig. 9c**).

5 DISCUSSION

To interpret the geochemical data, we considered samples collected at the base of the stratigraphic sequence (e.g., KF176-B), representative of the topmost portions of the magmatic reservoir at the moment of the eruption, while, in contrast, the top deposit horizons (e.g., KF176-O) represent the deepest part of the plumbing system that fed the eruption.

5.1 Reservoir Geochemistry

Melt inclusions entrapped in RP's haüyne occur as isolated, large inclusions and do not exhibit preferential planar alignments along crystal growth zones, making the identification of distinct MIAs impractical. As a result, the assumption that specific groups of MIs formed at the same reservoir conditions could not be validated through petrographic observations (e.g., Bodnar and Student, 2006; Esposito et al., 2014). However, the major element concentrations of haüyne-hosted MIs remain largely consistent across the stratigraphic sequence and between MIs located at different depths within the crystals. This suggests that the magma from which the MIs were entrapped was relatively chemically homogeneous at the time of haüyne crystallisation. A principal component analysis of major elements does not reveal substantial variability apart from a slight increase in the magmatic evolution of MIs entrapped at the top of the reservoir (**Supplementary Information**). Additionally, given the similarity of MI compositions with those of tephra glass and the independence from MI size, we also exclude a boundary layer effect that would have caused the inclusion to entrap a non-representative portion of melt (Faure and Schiano, 2005; Esposito et al., 2014).

The chemical compositions of embayments closely overlap those of MIs, implying that once haüyne began crystallising and trapping inclusions, the magma did not undergo significant compositional changes. This is further validated by the closeness of MIs major element composition to that of the pumice matrix glass than to bulk rock compositions (**Fig. 6**), indicating that MIs likely sampled the very final, most evolved magma before the eruption. However, slight depletions in Na_2O (0.05-1.32 wt.%) and Al_2O_3 (0.19-0.78 wt.%) and enrichment in K_2O (0.01-1.1 wt.%) are observed in MIs in comparison to pumice matrix glass. Haüyne preferentially incorporates Na_2O and Al_2O_3 over K_2O, and a post-entrapment crystallisation (PEC) at MI rims could potentially explain these chemical variations. A mass balance calculation suggests that a PEC of approximately 5 ±3 vol.% of the original MIs could account for the observed differences. However, this trend is not observed for CaO, another element preferentially incorporated by haüyne. This raises the question of whether PEC slightly influenced MI compositions or if the surrounding melt evolved due to the crystallisation of haüyne together with other phases, such as alkali feldspars. The rims of these feldspars tend toward the orthoclase endmember (**Supplementary Information**), suggesting progressive feldspar evolution, favouring K uptake over Na, relative to the timing of haüyne MI entrapment, while largely ignoring Ca. However, the chemical homogeneity of MIs glass (core to rim) and the absence of zonation around them in the host suggest that if PEC occurred, it played only a minor role in modifying MI compositions. A complete homogenisation of MI would have required, according to MI size and element diffusion, a timescale long enough to facilitate faceting processes, yet haüyne-hosted MIs in our dataset predominantly exhibit blunt or subrounded shapes, with fully faceted morphologies being rare (<2%).

A diffusion-dependent faceting process is observed in quartz-hosted MIs, even in the absence of PEC, with timescales ranging from tens to hundreds of years depending on the inclusion size (Gualda et al., 2012; Pamukcu et al., 2015; Ruefer et al., 2021). However, the MI size-faceting time relationship described by Gualda et al. (2012b) for quartz hosts cannot be directly applied to haüyne, as diffusion for elements other than silica must be considered. Additionally, we note that this speedometer is temperature-dependent and inferred for more viscous rhyolitic melts, which have lower diffusivities than the phonolitic-trachytic melts studied here. Higher elemental diffusivities enhance faceting rates, suggesting that blunt MIs likely had shorter residence times. The occurrence of sub-rounded MIs as small as 15 μm in diameter at the core of crystals therefore suggests that haüyne growth and inclusion entrapment occurred shortly before the eruption on geological timescales, which is further supported by the absence of microlites or growth rims within the MIs.

Comparison with chemical concentrations of MIs entrapped in mafic and alkali feldspars hosts (**Fig. 6**; Fontijn et al., 2013) reveals that haüyne-hosted MIs are more evolved, suggesting that differentiation processes had already occurred before haüyne crystallisation began. This interpretation is supported by trace element concentrations in the bulk pumice, which indicate a certain degree of crystallisation within the magmatic reservoir. The progressive enrichment of the most compatible trace elements with depth in the reservoir suggests advanced fractional crystallisation in its shallowest portions. Elements such as Ba, Sr, and Eu—compatible in alkali feldspars—were progressively sequestered during crystallisation, while incompatible elements accumulated in the residual melt. Considering an extreme scenario where the bulk partition coefficient (D) for highly incompatible elements (e.g., U and Th) approaches zero, the observed enrichment trends from the base to the top of the stratigraphic section correspond to a minimum of 60% Rayleigh fractional crystallisation. This implies that the whole-rock composition of the shallowest portions of the reservoir represents the 40% residual melt of the deeper magma (**Fig. 9d**).

A similar conclusion is reached when comparing trends of compatible versus incompatible trace elements for a range of pumice bulk partition coefficients (**Fig. 9c**). The only strong deviation from the general trend is observed in sample KF176-B, which exhibits significantly higher concentrations of Ba and other compatible elements like Sr than expected. While the lower SiO_2 and total alkali, and higher FeO_{tot} and compatible trace element concentrations in KF176-B could suggest a less evolved magma, its depletion in MgO and enrichment in incompatible elements relative to the rest of the deposit implies a more advanced stage of differentiation. This suggests that KF176-B may represent an older, separate, shallow mush zone in the reservoir, where in-situ equilibrium crystallisation was dominant rather than efficient crystal fractionation. Such a scenario would result in reduced fractionation of compatible elements, similar to processes observed at the uppermost parts of crystalline intrusions (Namur and Humphreys, 2018). Excluding KF176-B from the main trend results in a lower overall degree of fractional crystallisation (**Fig. 9c, d**). However, the crystal-poor topmost regions of the magmatic chamber exhibit the highest degrees of crystallisation, consistent with an effective fractionation process where crystals migrate toward the reservoir walls or settle in the crystal-rich lower portions (e.g., horizon KF176-O). This also supports the presence of a positive thermal gradient with depth. The substantial degree of crystallisation inferred from trace element trends contrasts with the major element homogeneity observed in MIs, which have compositions that closely resemble those of the pumice whole rock from the most evolved horizon, KF176-C (**Fig. 5**). This reinforces the idea that haüyne crystallised relatively late and predominantly trapped a residual melt at the final stages of magma evolution.

Experimental studies indicated that well-shaped, euhedral crystals growing at lower cooling rates tend to entrap a representative portion of parental melt in contrast to fast-growing skeletal or dendritic crystals, which often contain highly irregularly shaped melt inclusions (Faure and Schiano, 2005). Alternatively, crystallisation rate variability can create zonation of microscopic MI clusters within the host (Cooper et al., 2015). RP haüyne-hosted MIs are large and subspherical lacking distinctive zonation or clusters of MIs within individual crystals (Cooper et al., 2015). Morphologies such as mushroom-shaped MIs (*curvilinear* in Faure and Schiano, 2005), which were previously observed in olivine under single-stage, low-rate cooling experiments and linked to equilibrium growth (Faure and Schiano, 2005), are also commonly found in haüyne. This suggests that even the most irregular MIs can form at a constant, low undercooling, crystal growth, without the need for dissolution processes induced by local disequilibrium, such as fluid bubble interactions.

The stability of haüyne in phonolitic melts from Laacher See (Germany) and Tenerife (Spain) has been experimentally constrained to oxidising conditions (fO_2 > NNO buffer), pressures below 200-300 MPa, and temperatures between 750 and 900 °C (Berndt et al., 2001; Andújar et al., 2008; Baudouin and Parat, 2015). Berndt et al. (2001) observed a positive correlation between haüyne stability temperature, sulphur availability, and oxidising conditions in the parental melt. The sulphur accessibility thus likely plays a key role in haüyne stability and growth rate (Harms and Schmincke, 2000; Berndt et al., 2001; Cooper et al., 2015). The RP magma exhibits significantly higher sulphur content than other phonolitic systems, both in haüyne (e.g., ~4 wt.% less in Laacher See phenocrysts; Berndt et al., 2001) and melt (e.g., one order of magnitude lower in Laacher See MIs and matrix glasses; Harms and Schmincke, 2000). Berndt et al. (2001) inferred a late-stage differentiation of Laacher See haüyne, with oxidising conditions emerging shortly before eruption due to the injection of fresh, oxidised magma. Similarly, sulphur sparging from depth has been proposed as a mechanism accelerating haüyne growth in Tenerife phonolites (Cooper et al., 2015). In RP haüynes, sulphur concentration decreases toward shallower parts of the reservoir ($\Delta_{SO3} \approx$ 2600 ppm on average) mirroring trends in hosted MIs ($\Delta_{SO3} \approx$ 200 ppm on average) and pumice groundmass glass ($\Delta_{SO3} \approx$ 400 ppm). Among crystalline phases, haüyne likely played a role in sulphur depletion in the residual melt at shallower depths due to preferential uptake of sulphur (Harms and Schmincke, 2000). However, given the low abundance of crystallised haüyne (roughly estimated between 0.0 and 0.7 wt.%), it is unlikely to have solely buffered the sulphur content in the magma. Mass balance calculations suggest extremely low sulphur uptake (~38 ppm) in the topmost reservoir, whereas it would be significantly more effective in the deepest portions (600-800 ppm) due to increased haüyne crystallisation. Sulphur enrichment at depth may result from external inputs via gas sparging (Cooper et al., 2015) or mingling with a more oxidised, sulphur-rich magma (Harms and Schmincke, 2000; Berndt et al., 2001), enhancing haüyne stability in the deeper, more oxidised reservoir layers. These deep volatile sources were primarily enriched in sulphur while other volatiles remained constant (e.g., H_2O and CO_2) or showed opposite trends (e.g., Cl^-) in haüyne and hosted MIs. Additionally, small grains of pyrrhotite found included in alkali feldspar, biotite, and pyroxene (Fontijn et al., 2013), suggest that initial reducing conditions shifted during haüyne crystallisation, just before the eruption—similar to observations in Laacher See phonolites (Berndt et al., 2001).

Under ideal conditions, e.g., excluding any post-entrapment modifications, MIs can retain the volatile content of the original parental melt. However, volatile loss can occur, and as a rule of thumb, the highest volatile concentrations measured in a set of syn-entrapped MIs are considered the best estimate of original melt concentrations (e.g., Esposito et al., 2014). To estimate the water content of parental melt from haüyne-hosted MIs while accounting for uncertainties, we calculated an average based only on values above the third quartile of the dataset distribution, yielding 4.82 ±0.58 wt.% H_2O. Upon crystal cooling, if the rate is not sufficiently rapid, a single post-entrapment bubble may form due to differential contraction between the melt and the host crystal (Danyushevsky et al., 2002; Cannatelli et al., 2016; Rose-Koga et al., 2021 and reference therein), inducing volatile exsolution. Alternatively, if a volatile phase was already present in the original magma, a larger, pre-existing bubble could be trapped, typically resulting in greater size variability among co-genetic MIs (e.g., Davidson and Kamenetsky, 2007). The volume percentage occupied by single bubbles in haüyne-hosted MIs remains small and relatively constant across individual crystals, within the same stratigraphic horizon, and even throughout the deposit. This suggests that bubble formation occurred post-entrapment, rather than from pre-existing vapour phases in the melt (Danyushevsky et al., 2002; Moore et al., 2015; Cannatelli et al., 2016; Rose-Koga et al., 2021). This interpretation is further supported by the absence of fluid inclusions within haüyne crystals. Notably, bubble-free MIs are the most abundant, particularly in crystals from the shallower levels of the magmatic reservoir prior to the eruption, implying rapid ascent and cooling rates. In contrast, single bubbles are most common in MIs from the deeper portions of the reservoir, where longer cooling times may have allowed bubble formation during the eruption.

Shrinkage bubbles have the potential to induce water exsolution within them (e.g., Steele-MacInnis et al., 2017); however, no systematic water depletion trend was observed between bubble-hosting and bubble-free MIs, suggesting minimal impact on water loss. In contrast, studies of shrinkage bubbles indicate that they can contain between 30% and 90% of the originally dissolved CO_2 (Esposito et al., 2011; Moore et al., 2015; Rose-Koga et al., 2021 and references therein; Feignon et al., 2022), highlighting their importance in assessing total CO_2 concentrations in MIs. In the case of RP haüyne-hosted MIs, no molecular CO_2 was detected, even in bubble-free inclusions, suggesting that CO_2 levels were already low at the time of haüyne crystallisation. Nevertheless, significant CO_2 concentrations were measured in haüyne crystals themselves. This discrepancy could potentially be explained by crystal uptake during PEC, which could account for up to 90 ±50 ppm if ~5 vol.% of the MIs crystallised, while the effect on water content would be minimal. However, CO_2^{mol} present below FTIR detection limits or structural CO_2 may still represent residual CO_2 within MIs, meaning the estimated PEC contribution—and thus the inferred initial CO_2 concentrations for a hypothetical fully degassed tephra matrix—represent a maximum scenario.

The formation of multiple bubbles in microvesicular MIs may result from melt second boiling during PEC, volatile leakage upon ascent, heterogeneous nucleation, or the entrapment of an exsolved fluid phase (e.g., Danyushevsky et al., 2002; Cannatelli et al., 2016; Edmonds and Woods, 2018; Jorgenson et al., 2025). Notably, when present, such inclusions share the same texture as all other inclusions within the same crystal, suggesting that they record the full crystal's history rather than individual MI fracturing, decrepitation and volatile exsolution. The presence of a pre-entrapment exsolved fluid phase alone is unlikely to explain the formation of these MIs, given the absence of other clear evidence supporting this. Additionally, their overall abundance is minor and does not appear to be preferentially located at the top of the reservoir, as would be expected if a fluid phase had pervasively tapped this region. These bubbles often occupy the entire MI volume, which would imply a fully foamed magma within the reservoir during haüyne crystallisation—an unrealistic scenario, as such a magma would likely be unstable and prone to immediate eruption (Edmonds and Woods, 2018). While PEC could contribute to second boiling, estimated crystallised volume values do not support the degree of vesiculation required for widespread microvesicular MIs. Instead, heterogeneous bubble nucleation upon ascent, with some contribution from PEC, appears to be the most plausible explanation. Since bubble coalescence into a single bubble is a relatively fast process that can take seconds to minutes (e.g., Jorgenson et al., 2025 and references therein), we hypothesize that these MIs experienced a quenching rate intermediate between that of single-bubble and bubble-free MIs.

Embayments yield, on average, lower water concentrations than sealed inclusions (**Supplementary Table 2**) because melt in open embayments progressively equilibrates with the surrounding melt during ascent and is more likely to undergo diffusion-controlled re-equilibration during syn-eruptive degassing (Liu et al., 2007). The formation of large, tapered bubbles propagating from embayment outlets is associated with syn-eruptive melt supersaturation, which led to volatile degassing and vesiculation just before quenching (Ruefer et al., 2021). Bubbles are present within embayments either intruding from the outlet or forming as discrete bubbles. However, experimental observations have demonstrated that different bubble textures can be generated by the same decompression history (Hosseini et al., 2023). The concentration of bubbles at embayment outlets can be explained by the fact that melt inside the embayment does not respond to decompression disequilibrium in the same manner as the melt outside. Consequently, bubbles tend to nucleate in portions of embayments closer to the free melt and may migrate in and out of the embayment. The preservation of supersaturated conditions within embayments also inhibits decompression-induced microlite formation (Ruefer et al., 2021), as evidenced by the total absence of microlites in the embayments analysed in this study.

5.2 Thermobarometry

To characterise the pre-eruptive conditions of the magmatic reservoir in terms of temperature and pressure, we applied well-established petrological models. The entrapment temperature of haüyne-hosted MIs was estimated using the alkali feldspar-liquid geothermometer from Putirka (calibration error ±23 °C; Putirka, 2008). To assess equilibrium conditions, we calculated an equilibrium constant (Kd; Eq. (2) in Mollo et al., 2015), between each MI glass composition and the core, middle and rim portions of alkali feldspar crystals from the corresponding deposit horizon. The best correlation between the resulting Kd values and the measured equilibrium constant (Supplementary Material in Mollo et al., 2015) was found between MIs and the rims of alkali feldspars. Consequently, entrapment temperatures were estimated by pairing each MI with the rim of each crystal from the corresponding horizon, and the results were averaged to express variance. Temperatures range from ~938 to 1054 °C for MIs, with an average at 975 ±22 °C (**Fig. 10**). Overall, temperatures estimated with the Putirka (2008) geothermometer are comparable but slightly higher than those previously estimated with a Fe-Ti oxide pair (i.e., 925 °C; Fontijn et al., 2013). While these temperatures are comparable, it remains unclear whether the higher values derived from the alkali feldspar-melt thermometer result from the calibration of the equations used or from the fact that the two thermometers recorded different stages of the magmatic history and thermal conditions.

The saturation pressure at the moment of entrapment for a given water concentration was estimated using the solubility model from Di Matteo et al. (average relative error 12%; Di Matteo et al., 2004). To account for a potential CO_2 content in the parental melt up to 90 ppm, we also applied the MagmaSat model (**Supplementary Table 3**; Ghiorso and Gualda, 2015; Iacovino et al., 2021). Saturation pressures calculated using the Di Matteo et al. (2004) model range between 39 and 127 MPa (**Fig. 10**). However, considering only the highest recorded water concentrations as representative of the original melt conditions, an average pressure of 92 ± 15 MPa is obtained. Including CO_2 in the estimates yields higher saturation pressures, resulting in 144 ±28 MPa on average. However, we acknowledge that MagmaSat CO_2-free estimates tend to overestimate saturation pressures compared to the Di Matteo et al. (2004) model by up to 43 MPa for water contents ~5 wt.% (**Supplementary Table 2**), similar to other solubility models preferentially tested for calc-alkaline compositions (e.g., Di Matteo et al., 2004; Allison et al., 2019). This suggests that, while CO_2 was present, its influence on saturation pressure estimates was likely minimal.

Pressure estimations from solubility models can represent reservoir lithostatic pressures only in case of volatile saturation. The values obtained here are lower than previous estimates from the clinopyroxene-liquid barometer (i.e., 70-350 MPa; Fontijn et al., 2013). This wide range reflects the dependence of pyroxene-hosted MI pressures on water content, with the highest water concentrations yielding pressures considerably greater than those recorded for haüyne-hosted MIs. This could imply that the reservoir was stored at significant depths, at water-undersaturated conditions. However, clinopyroxene-hosted MIs likely formed earlier, as indicated by their less evolved compositions, and possibly at deeper crustal levels. No evidence from haüyne-hosted MIs suggests water saturation conditions during haüyne crystallisation, however, the potential occurrence of second boiling due to minor PEC implies conditions were not far from saturation. We interpret our estimates as a minimum storage lithostatic pressure during haüyne crystallisation, corresponding to a depth of 3.4 ± 0.6 km in the crust, assuming an average continental crust density of 2.7 $g \cdot cm^{-3}$.

5.3 Conceptual model

Based on observations from this and previous studies, we propose a conceptual model to describe the pre-eruptive conditions and evolution of the RP reservoir.

The RP reservoir likely differentiated from a deeper basaltic parental magma (Furman, 1995; Fontijn et al., 2013) through fractional crystallisation, producing a trachytic/phonolitic melt (**Fig. 11a**). However, as observed in other peralkaline systems along the EAR, where intermediate products are missing (e.g., Macdonald, 1987; Tadesse et al., 2019 and references therein), we do not exclude the possibility of crustal assimilation contributing to magmatic differentiation. This is supported by La/Nb values consistently above 1 (Plank, 2005).

Once stored in the upper crust, a temperature gradient promoted crystal fractionation, primarily in the shallower portions of the reservoir, leading to the crystallisation of mafic minerals (e.g., clinopyroxenes and biotite) and early alkali feldspars (**Fig. 11b**). Magmatic differentiation through fractional crystallisation proceeded over an extended period, as indicated by trace element patterns suggesting up to 50% fractional crystallisation and the presence of alkali feldspar crystals exceeding 2 mm in size. Crystals that formed near the reservoir roof were likely transported toward its walls and deeper regions. However, given the low crystal content in ash components and lapilli clasts, it is plausible that only a small fraction of these crystals was retained in the eruptible portion of the reservoir. Most crystals may have segregated from the magma, similar to the crystal-poor rhyolitic magmas that leave behind batholithic crystalline mushes (Bachmann and Bergantz, 2004). This is consistent with observations from other peralkaline systems in the EAR, where mush segregation rates can reach 10^{-1}-10^{-4} $km^3 \cdot yr^{-1}$ (Iddon et al., 2019).

Haüyne crystallisation likely occurred at shallower crustal depths than mafic mineral crystallisation, during a stage when the reservoir's major element chemistry had largely homogenised (**Fig. 11c**). Residence time at these depths must have been relatively short, as evidenced by the unfaceted shapes of MIs and the absence of breakdown or reaction rims around biotite crystals (Fontijn et al., 2013), which are known to be unstable to depressurisation-induced water loss (e.g., Fougnot et al., 1996).

A minimum storage depth of approximately 3.4 km is inferred under water-undersaturated conditions. Water content in RP melt inclusions is relatively low compared to the estimated volatile content at saturation for phonolitic magmas at crustal pressures (e.g., ~8 wt.% at 200 MPa; Carroll and Blank, 1997; Berndt et al., 2001) or values recorded in other EAR peralkaline magmas (e.g., Wilding et al., 1993; Iddon and Edmonds, 2020). However, it aligns with undersaturated values observed in other phonolitic magmas containing modal haüyne, such as the El Abrigo ignimbrite in Tenerife, Spain (Andújar et al., 2008). While shallow magma storage is often considered unusual, petrological evidence and direct observations (e.g., boreholes encountering magma pockets at Krafla, Iceland, and Menengai, Kenya; Papale and Garg, 2022), suggest that it may be more common than previously thought. Similar shallow storage depths have also been inferred for other phonolitic systems in divergent, convergent, and intraplate settings (e.g., Teide, Andújar et al., 2008; Andújar and Scaillet, 2012b; Vesuvius, Italy, Scaillet et al., 2008).

Haüyne stability in the deeper portions of the reservoir may have been influenced by more oxidising conditions. This could result from either (1) the input of fresh, oxidised magma or (2) the upward migration of a SO_3-rich volatile phase. In the first scenario, the fresh magma must have had a major element composition similar to that of the resident melt and a short residence time (according to crystallisation kinetics), given the lack of detectable changes in groundmass glass and alkali feldspar (and other phases) growth rims. The rare (<1% modal components) grey/banded pumice found in the lapilli fraction (Fontijn et al., 2011), which is crystal-rich and hosts plagioclase, has been inferred as evidence of mingling with intruding magma

(**Supplementary Table 2**). In the second scenario, evidence for a volatile phase sparging from depth includes sulphur enrichment in both haüyne crystals and the melt at the reservoir bottom. The volatile phase must have been sulphur-rich but depleted in other volatiles, as no enrichment trends are observed for other species. Whether driven by rapid magma accumulation or external volatile input, either process could have contributed to destabilising the system and initiating the unrest that culminated in the eruption (**Fig. 11c,d**; e.g., Caricchi et al., 2018; Jorgenson et al., 2024).

Pumice clasts in the finer-grained KF176-B horizon appear darker, softer, and more altered than those in overlying deposits. Reverse grading at the base of RP deposits is observed primarily at outcrops southeast of Rungwe and near the vent, where isopach thickness is also slightly greater (Fontijn et al., 2010b). This suggests an initial eruption phase of lower explosivity, producing a fine-grained lapilli fallout deposit primarily in the south, followed by a hiatus long enough to allow early alteration processes to affect the pumice glass. Major and trace element concentrations indicate that these products experienced a distinct evolution compared to the main RP magma, possibly tapping a shallow residual from previous activity. Subsequently, the peak in lithics in KF176-C may correspond to a conduit-clearing event in the eruption's initial stages, consistent with the observed reverse grading (Fontijn et al., 2011), before transitioning into the main explosive phase.

Comparative studies of phonolitic-trachytic systems suggest water-saturation alone is not definitive in triggering explosivity, while its proximity and relation with reservoir depth appear to be relevant factors in influencing eruptive explosivity (Andújar and Scaillet (2012a). In contrast, rheology at storage conditions does not appear to directly control eruption style, as peralkaline systems with similar viscosities have produced both effusive and highly explosive eruptions (Andújar and Scaillet, 2012a). At a given temperature high-alkali silicic magmas yield viscosities more than one order of magnitude lower than their sub-alkaline counterparts (Di

Genova et al., 2013). Low viscosities help decouple volatiles from magma and theoretically promote efficient outgassing and mildly explosive eruptions (Cassidy et al., 2018). For RP magmas at storage conditions, an average viscosity of $10^{3.45 \pm 0.33}$ Pa·s using the Giordano et al. (2008) model. At equivalent temperatures, these viscosities are comparable to those of other explosive phonolitic/trachytic melts (Andújar and Scaillet, 2012a) but also to those of lathitic or shoshonitic magmas that have produced Strombolian or lava-fountaining activity (Di Genova et al., 2013). Volatile loss during ascent significantly impacts magma viscosity. For RP magmas, decreasing water content to anhydrous conditions increases viscosity by up to four orders of magnitude (up to 10^6 Pa·s). Despite this increase, viscosities remain below general values for strain-induced brittle fragmentation (> 10^8 Pa·s; Papale, 1999). Additionally, the aphyric nature of RP pumice clasts and their low phenocryst content suggest that crystallinity had little influence on magma rheology (Dingwell et al., 1993).

Water content in the RP reservoir was relatively low but possibly close to saturation. The high bubble number density in pumice clasts (Cappelli et al., 2025) suggests that rapid ascent and syn-eruptive bubble nucleation significantly influenced magma rheology. Thus, conduit dynamics likely played a key role in preventing outgassing and driving brittle magma fragmentation, as observed in other relatively low-viscosity explosive eruptions (e.g., Houghton et al., 2004; Hughes et al., 2017).

6 CONCLUSIONS

We propose that the RP magma was stored at relatively shallow depths under conditions close to saturation. The injection of an S-rich gaseous phase into the reservoir likely induced haüyne crystallisation and contributed to system destabilisation. Shortly after, as inferred from the unfaceted nature of haüyne-hosted melt inclusions, the eruption commenced. The interplay between ponding depth and saturation conditions may have played a key role in driving explosivity. However, further investigations of conduit dynamics are needed to fully unravel the degassing and fragmentation processes that ultimately dictated the magma's eruptive behaviour beyond the conditions initially acquired at the reservoir level.

Across the East African Rift, several peralkaline silicic systems have produced violent eruptions, sometimes culminating in caldera-forming events while others have exhibited less violent effusive activity despite similar magmatic compositions (e.g., Leat, 1984b; Macdonald and Scaillet, 2006; White et al., 2012). Although the eruptive volumes of these explosive events are generally modest (~1 km^3 DRE max) compared to arc magmatism, the transitional nature of such systems still poses a significant hazard to densely populated regions. We emphasize the importance of a comprehensive assessment of pre-eruptive conditions, as individual parameters—such as water content or magma viscosity—may be insufficient to predict eruption style. Relying solely on these factors could lead to an underestimation of the explosive potential of a given volcanic system.

DATA AVAILABILITY STATEMENT

The data underlying this article are available in the article and in its online supplementary material. Additionally, the data underlying this article are available in EarthChem Library, at https://dx.doi.org/[doi]

FUNDING

This work was supported by an F.R.S.-FNRS Aspirant PhD studentship awarded to LC, and an F.R.S.-FNRS MIS [grant number F4515.20] awarded to KF. Samples were obtained during KF's doctoral thesis, funded by FWO Flanders. PW was founded by a F.R.S.-FNRS postdoctoral research fellowship. Isterre MicroAnalytical Plateforme (IMAP) in University Grenoble Alpes was funded by grants from: the European Research Council (ERC) under the European Union's Horizon H2020 research and innovation program (Synergy Grant MEET, grant agreement no.856555); Auvergne-Rhône-Alpes region (2020 AURA P3 - CPER 2015/2020).

ACKNOWLEDGEMENTS

The authors are grateful to Valentina Batanova and Valerie Magnin (IMAP laboratories, University Grenoble Alpes-Isterre; France) for technical support during EPMA data collection, Vinciane Debaille and Wendy Debouge (G-Time laboratory, Université Libre de Bruxelles; Belgium) for handling the mass spectrometry analyses and Aneta Slodczyk (CNRS-Orleans; France) for her assistance in FTIR analyses.

REFERENCES

Agrinier, P., Jendrzejewski, N., 2000. Overcoming problems of density and thickness measurements in FTIR volatile determinations: a spectroscopic approach. Contribution to Mineralogy and Petrology 139, 265–272.

Allison, C.M., Roggensack, K., Clarke, A.B., 2019. H2O–CO2 solubility in alkali-rich mafic magmas: new experiments at mid-crustal pressures. Contributions to Mineralogy and Petrology 174. https://doi.org/10.1007/s00410-019-1592-4

Andújar, J., Costa, F., Martí, J., Wolff, J.A., Carroll, M.R., 2008. Experimental constraints on the pre-eruptive conditions of the phonolitic magma from the caldera-forming the Abrigo eruption, Tenerife (Canary Islands). Chem Geol 257, 173–191. https://doi.org/10.1016/j.chemgeo.2008.08.012

Andújar, J., Scaillet, B., 2012a. Relationships between pre-eruptive conditions and eruptive styles of phonolite-trachyte magmas. Lithos 152, 122–131. https://doi.org/10.1016/j.lithos.2012.05.009

Andújar, J., Scaillet, B., 2012b. Experimental constraints on parameters controlling the difference in the eruptive dynamics of phonolitic magmas: The case of tenerife (Canary islands). Journal of Petrology 53, 1777–1806. https://doi.org/10.1093/petrology/egs033

Avanzinelli, R., Bindi, L., Menchetti, S., Conticelli, S., 2004. Crystallisation and genesis of peralkaline magmas from Pantelleria Volcano, Italy: An integrated petrological and crystal-chemical study. Lithos 73, 41–69. https://doi.org/10.1016/j.lithos.2003.10.007

Bachmann, O., Bergantz, G.W., 2004. On the origin of crystal-poor rhyolites: Extracted from batholithic crystal mushes. Journal of Petrology 45, 1565–1582. https://doi.org/10.1093/petrology/egh019

Baudouin, C., Parat, F., 2015. Role of volatiles (S, Cl, H2O) and silica activity on the crystallization of haüyne and nosean in phonolitic magmas (Eifel, Germany and Saghro, Morocco). American Mineralogist 100, 2308–2322. https://doi.org/10.2138/am-2015-5318

Behrens, H., Hahn, M., 2009. Trace element diffusion and viscous flow in potassium-rich trachytic and phonolitic melts. Chem Geol 259, 63–77. https://doi.org/10.1016/j.chemgeo.2008.10.014

Bellatreccia, F., Della Ventura, G., Piccinini, M., Cavallo, A., Brilli, M., 2009. H 2 O and CO 2 in minerals of the haüyne-sodalite group: an FTIR spectroscopy study . Mineral Mag 73, 399–413. https://doi.org/10.1180/minmag.2009.073.3.399

Berndt, J., Holtz, F., Koepke, J., 2001. Experimental constraints on storage conditions in the chemically zoned phonolitic magma chamber of the Laacher See volcano. Contributions to Mineralogy and Petrology 140, 469–486.

Biggs, J., Ayele, A., Fischer, T.P., Fontijn, K., Hutchison, W., Kazimoto, E., Whaler, K., Wright, T.J., 2021. Volcanic activity and hazard in the East African Rift Zone. Nat Commun. https://doi.org/10.1038/s41467-021-27166-y

Bodnar, J.R., Student, J.J., 2006. Melt inclusions in plutonic rocks: Petrography and microthermometry, in: James D. Webster (Ed.), Melt Inclusions in Plutonic Rocks. Short course Vol.36, Mineralogical Association of Canada, Montreal, Quebec, pp. 1–25.

Brooker, R.A., Kohn, S.C., Holloway, J.R., Mcmillan, P.F., Carroll, M.R., 1999. Solubility, speciation and dissolution mechanisms for CO_2 in melts on the $NaAlO_2$-SiO_2 join. Geochimica and Cosmochimica Acta 63, 3549–3565.

Cannatelli, C., Doherty, A.L., Esposito, R., Lima, A., De Vivo, B., 2016. Understanding a volcano through a droplet: A melt inclusion approach. J Geochem Explor 171, 4–19. https://doi.org/10.1016/j.gexplo.2015.10.003

Cappelli, L., Buono, G., Pappalardo, L., van Gerve, T., Namur, O., Sielenou, V., Ernst, G., Mbede, E., Kwelwa, S., Abdallah, E., Fontijn, K., 2025. Conduit dynamics of the Rungwe Pumice eruption (Tanzania): From storage to fragmentation of phonolitic-trachytic magmas. EarthArxiv Preprint [8672]-Accessed (03-01-2025).

Carey, S., Sparks, R.S.J., 1986. Quantitative models of the fallout and dispersal of tephra from volcanic eruption columns. Bull Volcanol 48, 109–125. https://doi.org/10.1007/BF01046546

Caricchi, L., Sheldrake, T.E., Blundy, J., 2018. Modulation of magmatic processes by CO2 flushing. Earth Planet Sci Lett 491, 160–171. https://doi.org/10.1016/j.epsl.2018.03.042

Carroll, M.R., Blank, J.G., 1997. The solubility of H_2O in phonolitic melts, American Mineralogist.

Cassidy, M., Manga, M., Cashman, K., Bachmann, O., 2018. Controls on explosive-effusive volcanic eruption styles. Nat Commun 9. https://doi.org/10.1038/s41467-018-05293-3

Castillo, P.R., Hilton, D.R., Halldórsson, S.A., 2014. Trace element and Sr-Nd-Pb isotope geochemistry of Rungwe Volcanic Province, Tanzania: Implications for a superplume source for East Africa Rift magmatism. Front Earth Sci (Lausanne) 2. https://doi.org/10.3389/feart.2014.00021

Cioni, R., 2000. Volatile content and degassing processes in the AD 79 magma chamber at Vesuvius (Italy). Contributions to Mineralogy and Petrology 140, 40–54. https://doi.org/10.1007/s004100000167

Cioni, R., Pistolesi, M., Rosi, M., 2015. Plinian and Subplinian Eruptions, in: The Encyclopedia of Volcanoes. Elsevier, pp. 519–535. https://doi.org/10.1016/b978-0-12-385938-9.00029-8

Cioni, R., Santacroce, R., Sbrana, A., 1999. Pyroclastic deposits as a guide for reconstructing the multi-stage evolution of the Somma-Vesuvius Caldera. Springer-Verlag.

Cooper, L.B., Bachmann, O., Huber, C., 2015. Volatile budget of Tenerife phonolites inferred from textural zonation of S-rich haüyne. Geology 43, 423–426. https://doi.org/10.1130/G36505.1

Danyushevsky, L. V., McNeill, A.W., Sobolev, A. V., 2002. Experimental and petrological studies of melt inclusions in phenocrysts from mantle-derived magmas: An overview of techniques, advantages and complications. Chem Geol 183, 5–24. https://doi.org/10.1016/S0009-2541(01)00369-2

Davidson, P., Kamenetsky, V.S., 2007. Primary aqueous fluids in rhyolitic magmas: Melt inclusion evidence for pre- and post-trapping exsolution. Chem Geol 237, 372–383. https://doi.org/10.1016/j.chemgeo.2006.07.009

Degruyter, W., Bachmann, O., Burgisser, A., Manga, M., 2012. The effects of outgassing on the transition between effusive and explosive silicic eruptions. Earth Planet Sci Lett 349–350, 161–170. https://doi.org/10.1016/j.epsl.2012.06.056

Devine, J.D., Gardner, J.E., Brack, H.P., Layne, G.D., Rutherford, M.J., 1995. Comparison of microanalytical methods for estimating H2O contents of silicic volcanic glasses. American Mineralogist 80, 319–328. https://doi.org/10.2138/am-1995-3-413

Di Genova, D., Romano, C., Hess, K.U., Vona, A., Poe, B.T., Giordano, D., Dingwell, D.B., Behrens, H., 2013. The rheology of peralkaline rhyolites from Pantelleria Island. Journal of Volcanology and Geothermal Research 249, 201–216. https://doi.org/10.1016/j.jvolgeores.2012.10.017

Di Matteo, V., Carroll, M.R., Behrens, H., Vetere, F., Brooker, R.A., 2004. Water solubility in trachytic melts. Chem Geol 213, 187–196. https://doi.org/10.1016/j.chemgeo.2004.08.042

Dingwell, D.B., 1996. Volcanic Dilemma: Flow or Blow? Science (1979) 273, 1054–1055.

Dingwell, D.B., Bagdassarov, N.S., Bussod, G.Y., Webb, S.L., 1993. Magma Rheology, in: Luth, R.W. (Ed.), Experiments at High Pressures and Applications to the Earth's Mantle, Short Course Handbook. Mineralogical Association of Canada, Edmonton, Alberta, pp. 131–196.

Dingwell, D.B., Webb, S.L., 1989. Structural Relaxation in Silicate Melts and Non-Newtonian Melt Rheology in Geologic Processes. Phys Chem Miner 16, 508–516.

Ebinger, C.J., Deino, A.L., Drake, E., Tesha, A.L., 1989. Chronology of volcanism and rift basin propagation: Rungwe Volcanic Province, East Africa. Journal of Geophysical Research 94, 15785–15803.

Ebinger, C.J., Deino, A.L., Tesha, A.L., Becker, T., Ring, U., 1993. Tectonic controls on rift basin morphology: evolution of the northern Malawi (Nyasa) Rift. J Geophys Res 98. https://doi.org/10.1029/93jb01392

Ebinger, C.J., Keir, D., Bastow, I.D., Whaler, K., Hammond, J.O.S., Ayele, A., Miller, M.S., Tiberi, C., Hautot, S., 2017. Crustal Structure of Active Deformation Zones in Africa: Implications for Global Crustal Processes. Tectonics. https://doi.org/10.1002/2017TC004526

Edmonds, M., Woods, A.W., 2018. Exsolved volatiles in magma reservoirs. Journal of Volcanology and Geothermal Research. https://doi.org/10.1016/j.jvolgeores.2018.10.018

Esposito, R., Badescu, K., Steele-MacInnis, M., Cannatelli, C., De Vivo, B., Lima, A., Bodnar, R.J., Manning, C.E., 2018. Magmatic evolution of the Campi Flegrei and Procida volcanic fields, Italy, based on interpretation of data from well-constrained melt inclusions. Earth Sci Rev 185, 325–356. https://doi.org/10.1016/j.earscirev.2018.06.003

Esposito, R., Bodnar, R.J., Danyushevsky, L. V., De vivo, B., Fedele, L., Hunter, J., Lima, A., Shimizu, N., 2011. Volatile evolution of magma associated with the solchiaro eruption in the Phlegrean Volcanic District (Italy). Journal of Petrology 52, 2431–2460. https://doi.org/10.1093/petrology/egr051

Esposito, R., Hunter, J., Schiffbauer, J.D., Shimizu, N., Bodnar, R.J., 2014. An assessment of the reliability of melt inclusions as recorders of the pre-eruptive volatile content of magmas. American Mineralogist 99, 976–998. https://doi.org/10.2138/am.2014.4574

Faure, F., Schiano, P., 2005. Experimental investigation of equilibration conditions during forsterite growth and melt inclusion formation. Earth Planet Sci Lett 236, 882–898. https://doi.org/10.1016/j.epsl.2005.04.050

Feignon, J.G., Cluzel, N., Schiavi, F., Moune, S., Roche, O., Clavero, J., Schiano, P., Auxerre, M., 2022. High CO2 content in magmas of the explosive andesitic Enco eruption of Mocho-Choshuenco volcano (Chile). Bull Volcanol 84. https://doi.org/10.1007/s00445-022-01550-y

Fontijn, K., Delvaux, D., Ernst, G.G.J., Kervyn, M., Mbede, E., Jacobs, P., 2010a. Tectonic control over active volcanism at a range of scales: Case of the Rungwe Volcanic Province, SW Tanzania; and hazard implications. Journal of African Earth Sciences 58, 764–777. https://doi.org/10.1016/j.jafrearsci.2009.11.011

Fontijn, K., Elburg, M.A., Nikogosian, I.K., van Bergen, M.J., Ernst, G.G.J., 2013. Petrology and geochemistry of Late Holocene felsic magmas from Rungwe volcano (Tanzania), with implications for trachytic Rungwe Pumice eruption dynamics. Lithos 177, 34–53. https://doi.org/10.1016/j.lithos.2013.05.012

Fontijn, K., Ernst, G.G.J., Bonadonna, C., Elburg, M.A., Mbede, E., Jacobs, P., 2011. The ~4-ka Rungwe Pumice (South-Western Tanzania): A wind-still Plinian eruption. Bull Volcanol 73, 1353–1368. https://doi.org/10.1007/s00445-011-0486-8

Fontijn, K., Ernst, G.G.J., Elburg, M.A., Williamson, D., Abdallah, E., Kwelwa, S., Mbede, E., Jacobs, P., 2010b. Holocene explosive eruptions in the Rungwe Volcanic Province, Tanzania. Journal of Volcanology and Geothermal Research 196, 91–110. https://doi.org/10.1016/j.jvolgeores.2010.07.021

Fontijn, K., McNamara, K., Zafu Tadesse, A., Pyle, D.M., Dessalegn, F., Hutchison, W., Mather, T.A., Yirgu, G., 2018. Contrasting styles of post-caldera volcanism along the

Main Ethiopian Rift: Implications for contemporary volcanic hazards. Journal of Volcanology and Geothermal Research 356, 90–113. https://doi.org/10.1016/j.jvolgeores.2018.02.001

Fontijn, K., Williamson, D., Mbede, E., Ernst, G.G.J., 2012. The Rungwe Volcanic Province, Tanzania - A volcanological review. Journal of African Earth Sciences 63, 12–31. https://doi.org/10.1016/j.jafrearsci.2011.11.005

Fougnot, J., Pichavant, M., Barbey, P., 1996. Biotite resorption in dacite lavas from northeastern Algeria. European Journal of Mineralogy 8, 625–638.

Furman, T., 1995. Melting of metasomatized subcontinental lithosphere: undersaturated mafic lavas from Rungwe, Tanzania, Contrib Mineral Petrol. Springer-Verlag.

Garcin, Y., Williamson, D., Taieb, M., Vincens, A., Mathé, P.E., Majule, A., 2006. Centennial to millennial changes in maar-lake deposition during the last 45,000 years in tropical Southern Africa (Lake Masoko, Tanzania). Palaeogeogr Palaeoclimatol Palaeoecol 239, 334–354. https://doi.org/10.1016/j.palaeo.2006.02.002

Ghiorso, M.S., Evans, B.W., 2008. Thermodynamics of rhombohedral oxide solid solutions and a revision of the Fe-Ti two-oxide geothermometer and oxygen-barometer. Am J Sci 308, 957–1039. https://doi.org/10.2475/09.2008.01

Ghiorso, M.S., Gualda, G.A.R., 2015. An H2O–CO2 mixed fluid saturation model compatible with rhyolite-MELTS. Contributions to Mineralogy and Petrology 169. https://doi.org/10.1007/s00410-015-1141-8

Giordano, D., Russell, J.K., Dingwell, D.B., 2008. Viscosity of magmatic liquids: A model. Earth Planet Sci Lett 271, 123–134. https://doi.org/10.1016/j.epsl.2008.03.038

Gonnermann, H.M., 2015. Magma fragmentation. Annu Rev Earth Planet Sci 43, 431–458. https://doi.org/10.1146/annurev-earth-060614-105206

Gonnermann, H.M., Manga, M., 2007. The fluid mechanics inside a volcano. Annu Rev Fluid Mech. https://doi.org/10.1146/annurev.fluid.39.050905.110207

Gualda, G.A.R., Pamukcu, A.S., Ghiorso, M.S., Anderson, A.T., Sutton, S.R., Rivers, M.L., 2012. Timescales of Quartz crystallization and the longevity of the Bishop Giant Magma body. PLoS One 7. https://doi.org/10.1371/journal.pone.0037492

Harkin, D.A., 1960. The Rungwe Volcanics at the Northern End of Lake Nyasa, 1st ed. Government Printer.

Harms, E., Schmincke, H.-U., 2000. Volatile composition of the phonolitic Laacher See magma (12,900 yr BP): implications for syn-eruptive degassing of S, F, Cl and H 2 O. Contrib Mineral Petrol 138, 84–98.

Houghton, B.F., Wilson, C.J.N., Del Carlo, P., Coltelli, M., Sable, J.E., Carey, R., 2004. The influence of conduit processes on changes in style of basaltic Plinian eruptions: Tarawera 1886 and Etna 122 BC. Journal of Volcanology and Geothermal Research 137, 1–14. https://doi.org/10.1016/j.jvolgeores.2004.05.009

Hughes, E.C., Neave, D.A., Dobson, K.J., Withers, P.J., Edmonds, M., 2017. How to fragment peralkaline rhyolites: Observations on pumice using combined multi-scale 2D and 3D imaging. Journal of Volcanology and Geothermal Research 336, 179–191. https://doi.org/10.1016/j.jvolgeores.2017.02.020

Hutchison, W., Mather, T.A., Pyle, D.M., Boyce, A.J., Gleeson, M.L.M., Yirgu, G., Blundy, J.D., Ferguson, D.J., Vye-Brown, C., Millar, I.L., Sims, K.W.W., Finch, A.A., 2018. The evolution of magma during continental rifting: New constraints from the isotopic and trace element signatures of silicic magmas from Ethiopian volcanoes. Earth Planet Sci Lett 489, 203–218. https://doi.org/10.1016/j.epsl.2018.02.027

Hutchison, W., Pyle, D.M., Mather, T.A., Yirgu, G., Biggs, J., Cohen, B.E., Barfod, D.N., Lewi, E., 2016. The eruptive history and magmatic evolution of Aluto volcano: new insights into silicic peralkaline volcanism in the Ethiopian rift. Journal of Volcanology and Geothermal Research 328, 9–33. https://doi.org/10.1016/j.jvolgeores.2016.09.010

Iacovino, K., Matthews, S., Wieser, P.E., Moore, G.M., Bégué, F., 2021. VESIcal Part I: An Open-Source Thermodynamic Model Engine for Mixed Volatile (H2O-CO2) Solubility in Silicate Melts. Earth and Space Science 8. https://doi.org/10.1029/2020EA001584

Iddon, F., Edmonds, M., 2020. Volatile-Rich Magmas Distributed Through the Upper Crust in the Main Ethiopian Rift. Geochemistry, Geophysics, Geosystems 21. https://doi.org/10.1029/2019GC008904

Iddon, F., Jackson, C., Hutchison, W., Fontijn, K., Pyle, D.M., Mather, T.A., Yirgu, G., Edmonds, M., 2019. Mixing and Crystal Scavenging in the Main Ethiopian Rift Revealed by Trace Element Systematics in Feldspars and Glasses. Geochemistry, Geophysics, Geosystems 20, 230–259. https://doi.org/10.1029/2018GC007836

Jeffery, A.J., Gertisser, R., 2018. Peralkaline Felsic Magmatism of the Atlantic Islands. Front Earth Sci (Lausanne). https://doi.org/10.3389/feart.2018.00145

Jochum, K.P., Stoll, B., Herwig, K., Willbold, M., Hofmiann, A.W., Amini, M., Aarburg, S., Abouchami, W., Hellebrand, E., Mocek, B., Raczek, I., Stracke, A., Alard, O., Bouman, C., Becker, S., Dücking, M., Brätz, H., Klemd, R., De Bruin, D., Canil, D., Cornell, D., De Hoog, C.J., Dalpé, C., Danyushevshy, L., Eisenhauer, A., Gao, Y., Snow, J.E., Groschopf, N., Günther, D., Latkoczy, C., Guillong, M., Hauri, E.H., Höfer, H.E., Lahaye, Y., Horz, K., Jacob, D.E., Kasemann, S.A., Kent, A.J.R., Ludwig, T., Zack, T., Mason, P.R.D., Meixner, A., Rosner, M., Misawa, K., Nash, B.P., Pfänder, J., Premo, W.R., Sun, W.D., Tiepolo, M., Vannucci, R., Vennemann, T., Wayne, D., Woodhead, J.D., 2006. MPI-DING reference glasses for in situ microanalysis: New reference values for element concentrations and isotope ratios. Geochemistry, Geophysics, Geosystems 7. https://doi.org/10.1029/2005GC001060

Jorgenson, C., Caricchi, L., Chiaradia, M., Ágreda-López, M., Giordano, G., 2024. Rapid accumulation and ascent precedes caldera forming eruption of low viscosity magma. Contributions to Mineralogy and Petrology 179. https://doi.org/10.1007/s00410-023-02091-z

Jorgenson, C., Stuckelberger, M.E., Fevola, G., Falkenberg, G., Kaiser, T., Wilde, F., Weber, G., Giordano, G., Caricchi, L., 2025. A myriad of melt inclusions: a 3D analysis of melt inclusions reveals the gas rich magma reservoir of Colli Albani Volcano (Italy). Journal of Petrology. https://doi.org/10.1093/petrology/egaf012/8003508

Keller, J., Ryan, W.B.F., Ninkovich, D., Altherr, R., 1978. Explosive volcanic activity in the Mediterranean over the past 200,000 yr as recorded in deep-sea sediments. Bulletin of the Geological Society of America 89, 591–604. https://doi.org/10.1130/0016-7606(1978)89<591:EVAITM>2.0.CO;2

Lange, R.A., 1997. A revised model for the density and thermal expansivity of K_2O-Na_2O-CaO-MgO-Al_2O_3-SiO_2 liquids from 700 to 1900 K: extension to crustal magmatic temperatures. Contributions to Mineralogy and Petrology 130, 1–11. https://doi.org/10.1007/s004100050345

Lange, R.A., Carmichael, I.S.E., 1987. Densities of Na_2O-K_2O-CaO-MgO-FeO-Fe_2O_3-Al_2O_3-TiO_2-SiO_2 liquids: New measurements and derivated partial molar properties. Geochim Cosmochim Acta 51, 2931–2946.

Leat, P.T., 1984a. Geological evolution of the trachytic caldera volcano Menengai, Kenya Rift Valley. J Geol Soc London 141, 1057–1069. https://doi.org/10.1144/gsjgs.141.6.1057

Leat, P.T., 1984b. Geological evolution of the trachytic caldera volcano Menengai, Kenya Rift Valley. J Geol Soc London 141, 1057–1069. https://doi.org/10.1144/gsjgs.141.6.1057

Liu, Y., Anderson, A.T., Wilson, C.J.N., 2007. Melt pockets in phenocrysts and decompression rates of silicic magmas before fragmentation. J Geophys Res Solid Earth 112. https://doi.org/10.1029/2006JB004500

Macdonald, R., 1987. Quaternary peralkaline silicic rocks and caldera volcanoes of Kenya. Geol Soc Spec Publ 30, 313–333. https://doi.org/10.1144/GSL.SP.1987.030.01.15

Macdonald, R., Scaillet, B., 2006. The central Kenya peralkaline province: Insights into the evolution of peralkaline salic magmas. Lithos 91, 59–73. https://doi.org/10.1016/j.lithos.2006.03.009

Mahood, G.A., 1984. Pyroclastic Rocks and Calderas Associated With Strongly Peralkaline Magmatism. J Geophys Res 89, 8540–8552.

McDonough, W.F., Sun, S. -s., 1995. The Composition of Earth. Chem Geol 120, 223–253.

Mollo, S., Masotta, M., Forni, F., Bachmann, O., De Astis, G., Moore, G., Scarlato, P., 2015. A K-feldspar-liquid hygrometer specific to alkaline differentiated magmas. Chem Geol 392, 1–8. https://doi.org/10.1016/j.chemgeo.2014.11.010

Moore, L.R., Gazel, E., Tuohy, R., Lloyd, A.S., Esposito, R., Steele-MacInnis, M., Hauri, E.H., Wallace, P.J., Plank, T., Bodnar, R.J., 2015. Bubbles matter: An assessment of the contribution of vapor bubbles to melt inclusion volatile budgets. American Mineralogist 100, 806–823. https://doi.org/10.2138/am-2015-5036

Morizet, Y., Brooker, R.A., Iacono-Marziano, G., Kjarsgaard, B.A., 2013. Quantification of dissolved CO2 in silicate glasses using micro-Raman spectroscopy. American Mineralogist 98, 1788–1802. https://doi.org/10.2138/am.2013.4516

Namur, O., Humphreys, M.C.S., 2018. Trace element constraints on the differentiation and crystal mush solidification in the Skaergaard intrusion, Greenland. Journal of Petrology 59, 387–418. https://doi.org/10.1093/petrology/egy032

Newhall, C.G., Self, S., 1982. The volcanic explosivity index (VEI): an estimate of the explosive magnitude for historical eruptions. J Geophys Res 87, 1231–1238.

Nichols, A.R.L., Wysoczanski, R.J., 2007. Using micro-FTIR spectroscopy to measure volatile contents in small and unexposed inclusions hosted in olivine crystals. Chem Geol 242, 371–384. https://doi.org/10.1016/j.chemgeo.2007.04.007

Ochs III, F.A., Lange, R.A., 1999. The Density of Hydrous Magmatic Liquids. Science (1979) 283, 1314–1317. https://doi.org/DOI: 10.1126/science.283.5406.1314

Pamukcu, A.S., Gualda, G.A.R., Bégué, F., Gravley, D.M., 2015. Melt inclusion shapes: Timekeepers of short-lived giant magma bodies. Geology 43, 947–950. https://doi.org/10.1130/G37021.1

Papale, P., 1999. Strain-induced magma fragmentation in explosive eruptions. Nature 397, 425–428.

Papale, P., Garg, D., 2022. Big volcano science: needs and perspectives. Bull Volcanol 84. https://doi.org/10.1007/s00445-022-01524-0

Plank, T., 2005. Constraints from Thorium/Lanthanum on sediment recycling at subduction zones and the evolution of the continents. Journal of Petrology. https://doi.org/10.1093/petrology/egi005

Putirka, K.D., 2008. Thermometers and barometers for volcanic systems. Rev Mineral Geochem 69, 61–120. https://doi.org/10.2138/rmg.2008.69.3

Richet, P., Whittington, A., Holtz, F., Behrens, H., Ohlhorst, S., Wilke, M., 2000. Water and the density of silicate glasses. Contributions to Mineralogy and Petrology 138, 337–347. https://doi.org/10.1007/s004100050567

Rose-Koga, E.F., Bouvier, A.S., Gaetani, G.A., Wallace, P.J., Allison, C.M., Andrys, J.A., Angeles de la Torre, C.A., Barth, A., Bodnar, R.J., Bracco Gartner, A.J.J., Butters, D., Castillejo, A., Chilson-Parks, B., Choudhary, B.R., Cluzel, N., Cole, M., Cottrell, E., Daly, A., Danyushevsky, L. V., DeVitre, C.L., Drignon, M.J., France, L., Gaborieau, M., Garcia, M.O., Gatti, E., Genske, F.S., Hartley, M.E., Hughes, E.C., Iveson, A.A., Johnson, E.R., Jones, M., Kagoshima, T., Katzir, Y., Kawaguchi, M., Kawamoto, T., Kelley, K.A., Koornneef, J.M., Kurz, M.D., Laubier, M., Layne, G.D., Lerner, A., Lin, K.Y., Liu, P.P., Lorenzo-Merino, A., Luciani, N., Magalhães, N., Marschall, H.R., Michael, P.J., Monteleone, B.D., Moore, L.R., Moussallam, Y., Muth, M., Myers, M.L., Narváez, D.F., Navon, O., Newcombe, M.E., Nichols, A.R.L., Nielsen, R.L., Pamukcu, A., Plank, T., Rasmussen, D.J., Roberge, J., Schiavi, F., Schwartz, D., Shimizu, K., Shimizu, N., Thomas, J.B., Thompson, G.T., Tucker, J.M., Ustunisik, G., Waelkens, C., Zhang, Y., Zhou, T., 2021. Silicate melt inclusions in the new millennium: A review of recommended practices for preparation, analysis, and data presentation. Chem Geol 570. https://doi.org/10.1016/j.chemgeo.2021.120145

Ruefer, A.C., Befus, K.S., Thompson, J.O., Andrews, B.J., 2021. Implications of Multiple Disequilibrium Textures in Quartz-Hosted Embayments. Front Earth Sci (Lausanne) 9. https://doi.org/10.3389/feart.2021.742895

Saria, E., Calais, E., Stamps, D.S., Delvaux, D., Hartnady, C.J.H., 2014. Present-day kinematics of the East African Rift. J Geophys Res Solid Earth 119, 3584–3600. https://doi.org/10.1002/2013JB010901

Scaillet, B., Pichavant, M., Cioni, R., 2008. Upward migration of Vesuvius magma chamber over the past 20,000 years. Nature 455, 216–219. https://doi.org/10.1038/nature07232

Shea, T., 2017. Bubble nucleation in magmas: A dominantly heterogeneous process? Journal of Volcanology and Geothermal Research. https://doi.org/10.1016/j.jvolgeores.2017.06.025

Sparks, R.S.J., 1978. The dynamics of bubble formation and growth in magmas: a review and analysis. Journal of Volcanology and Geothermal Research 3, 1–37.

Steele-MacInnis, M., Esposito, R., Moore, L.R., Hartley, M.E., 2017. Heterogeneously entrapped, vapor-rich melt inclusions record pre-eruptive magmatic volatile contents. Contributions to Mineralogy and Petrology 172. https://doi.org/10.1007/s00410-017-1343-3

Stern, R.J., 2002. Subduction zones. Reviews of Geophysics 40, 3-1-3–38. https://doi.org/10.1029/2001RG000108

Stolper, E., 1982. Water in silicate glasses: An infrared spectroscopic study. Contributions to Mineralogy and Petrology 81, 1–17. https://doi.org/10.1007/BF00371154

Tadesse, A.Z., Ayalew, D., Pik, R., Yirgu, G., Fontijn, K., 2019. Magmatic evolution of the Boku Volcanic Complex, Main Ethiopian Rift. Journal of African Earth Sciences 149, 109–130. https://doi.org/10.1016/j.jafrearsci.2018.08.003

Taylor, D., 1967. The Sodalite Group of Minerals, Contr. Mineral. and Petrol.

von Aulock, F.W., Kennedy, B.M., Schipper, C.I., Castro, J.M., E. Martin, D., Oze, C., Watkins, J.M., Wallace, P.J., Puskar, L., Bégué, F., Nichols, A.R.L., Tuffen, H., 2014. Advances in Fourier transform infrared spectroscopy of natural glasses: From sample preparation to data analysis. Lithos 206–207, 52–64. https://doi.org/10.1016/j.lithos.2014.07.017

Wadge, G., Biggs, J., Lloyd, R., Kendall, J.M., 2016. Historical volcanism and the state of stress in the east African rift system. Front Earth Sci (Lausanne) 4. https://doi.org/10.3389/feart.2016.00086

Walker, G.P.L., 1981. Plinian Eruptions and Their Products. Bull. Volcanol 44.

Wallace, P.A., Otieno, V., Godec, P., Njoroge, R.W., Tubula, M.S., Cappelli, L., Kamau, P.M., Nomade, S., Mariita, N.O., Fontijn, K., 2025. Temporal and spatial evolution of explosive silicic peralkaline eruptions at the Olkaria Volcanic Complex and Longonot volcano in the Southern Kenya Rift. Journal of Volcanology and Geothermal Research 108275. https://doi.org/10.1016/j.jvolgeores.2025.108275

White, J.C., Espejel-García, V. V., Anthony, E.Y., Omenda, P., 2012. Open System evolution of peralkaline trachyte and phonolite from the Suswa volcano, Kenya rift. Lithos 152, 84–104. https://doi.org/10.1016/j.lithos.2012.01.023

Wieser, P.E., Petrelli, M., Lubbers, J., Wieser, E., Özaydın, S., Kent, A.J.R., Till, C.B., 2022. Thermobar: An open-source Python3 tool for thermobarometry and hygrometry. Volcanica 5, 349–384. https://doi.org/10.30909/vol.05.02.349384

Wilding, M.C., Macdonald, R., Davies, J.E., Falliek, A.E., 1993. Volatile characteristics of peralkaline rhyolites from Kenya: an ion microprobe, infrared spectroscopic and hydrogen isotope study. Contrib Mineral Petrol 114, 26–275.

Williams, L.A.J., Macdonald, R., Chapman, G.R., 1984. Late Quaternary caldera volcanoes of the Kenya Rift Valley. J Geophys Res 89, 8553–8570. https://doi.org/10.1029/JB089iB10p08553

Wysoczanski, R., Tani, K., 2006. Spectroscopic FTIR imaging of water species in silicic volcanic glasses and melt inclusions: An example from the Izu-Bonin arc. Journal of Volcanology and Geothermal Research 156, 302–314. https://doi.org/10.1016/j.jvolgeores.2006.03.024

FIGURE CAPTIONS

Fig. 1: **a)** Location of the Rungwe Volcanic Province (*yellow box*) at the junction between the Eastern and Western branches of the EAR. Major rift faults (*red lines*) and volcanoes (*red triangles*) are indicated; **b)** shaded relief map of the RVP. The extension of the 25 cm isopach of the Rungwe Pumice fallout deposit is indicated by the red, dashed line (modified after Fontijn et al., 2011) while the location of the type section KF176 is indicated with the yellow star (12 m resolution DEM data: ASF DAAC, ALOS PALSAR_RTC_High res 2010; © JAXA/METI).

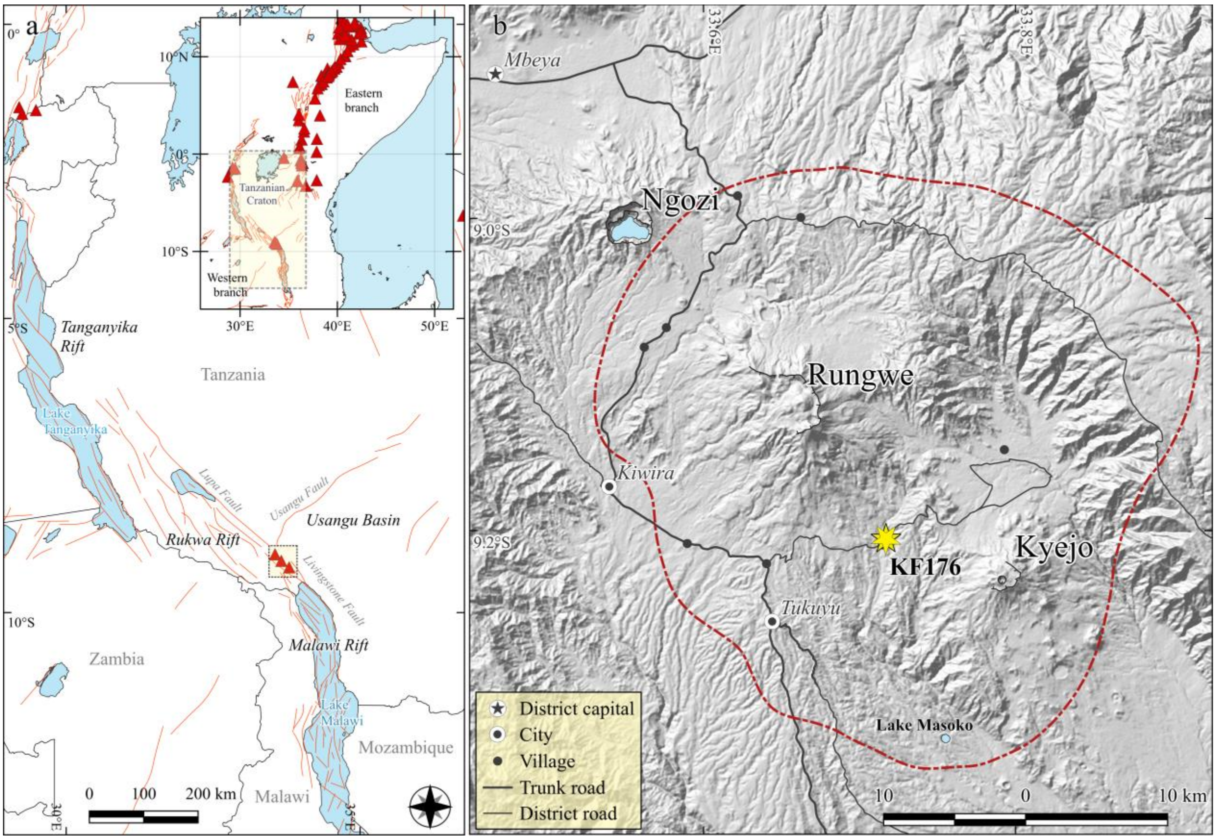

Fig. 2: Typical appearance of FTIR spectra for haüyne crystals and MIs volcanic glasses from our sample set. The main peaks for total water, molecular water, CO_2 and SO_4 are reported, while the inset zooms into the Near-IR region where the small molecular water and OH^- peaks are found.

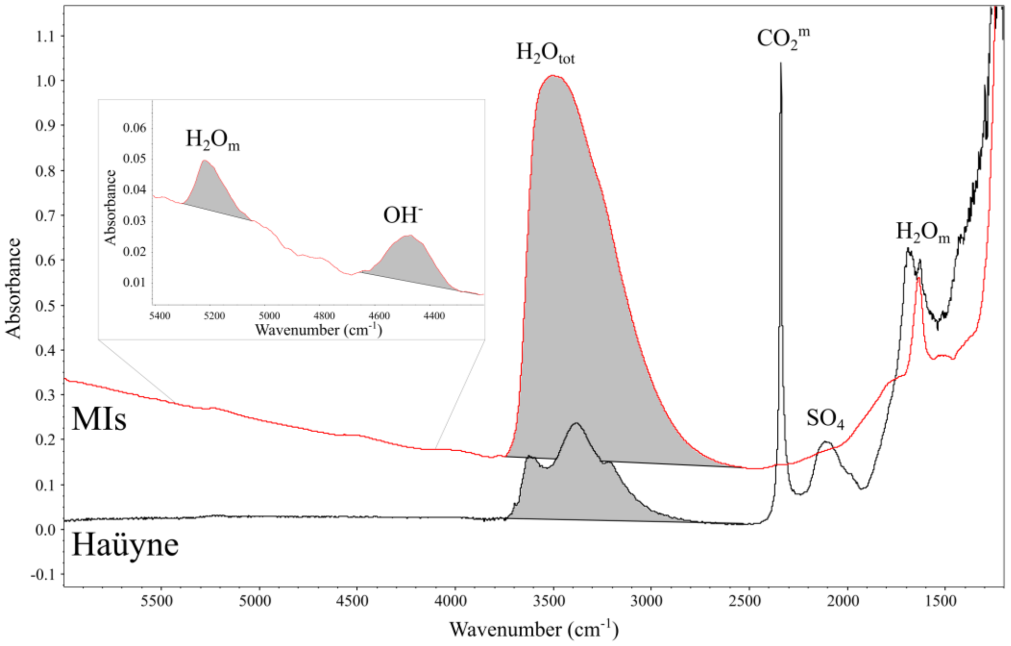

Fig. 3: Variations of componentry abundance across the Rungwe Pumice deposit for the medium and coarse ash grain sizes.

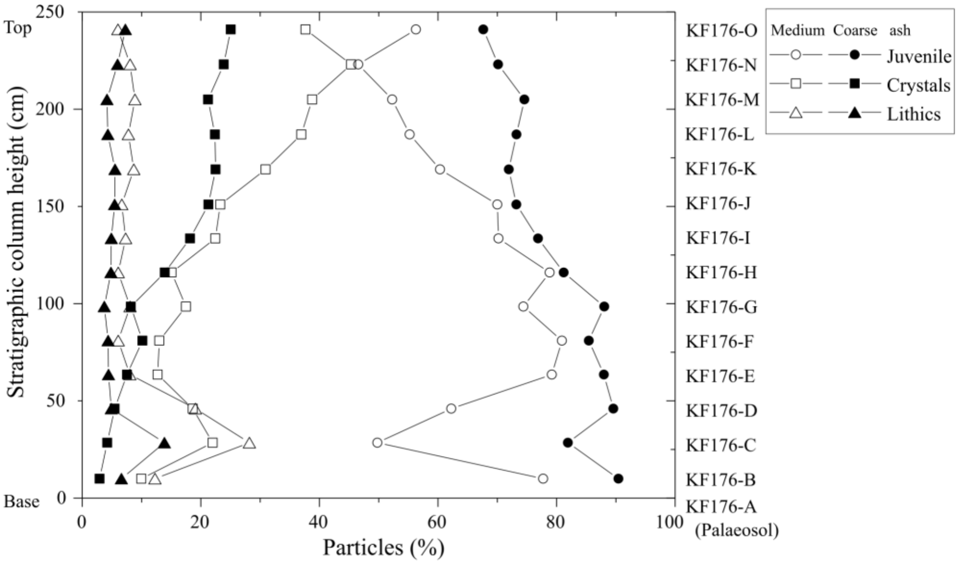

Fig. 4: Panels **a)** to **f)** show haüyne crystals hosting various MI types, including **a)** ellipsoidal single-bubble or bubble-free MIs; **a)** and **b)** mushroom-shaped embayment; **c)** microvesicular MI; **d)** large, sub-planar MIs; **e)** elongated MIs hosting multiple bubbles of variable size; **f)** embayment hosting several large bubbles connected to the outside and microvesicular in its innermost portions. Panels **g)** and **h)** illustrate the relationship between MI and bubble volumes

for different bubble-hosting MI types. For each multiple-bubble MIs, the total bubble volume is considered as the sum of all individual bubble volumes within it, while for microvesicular MIs, individual bubble volumes are shown. **g)** Scatter plot showing the linear relationship between MI and bubble volumes. Linear trends are represented by dashed black and solid red lines for single- and multiple-bubble MIs, respectively; **h)** Box-and-whisker plot displaying the statistical distribution of bubble volume occupancy for different MI types. The horizontal line represents the median, while whiskers enclose 90% of the dataset, and circles indicate outliers.

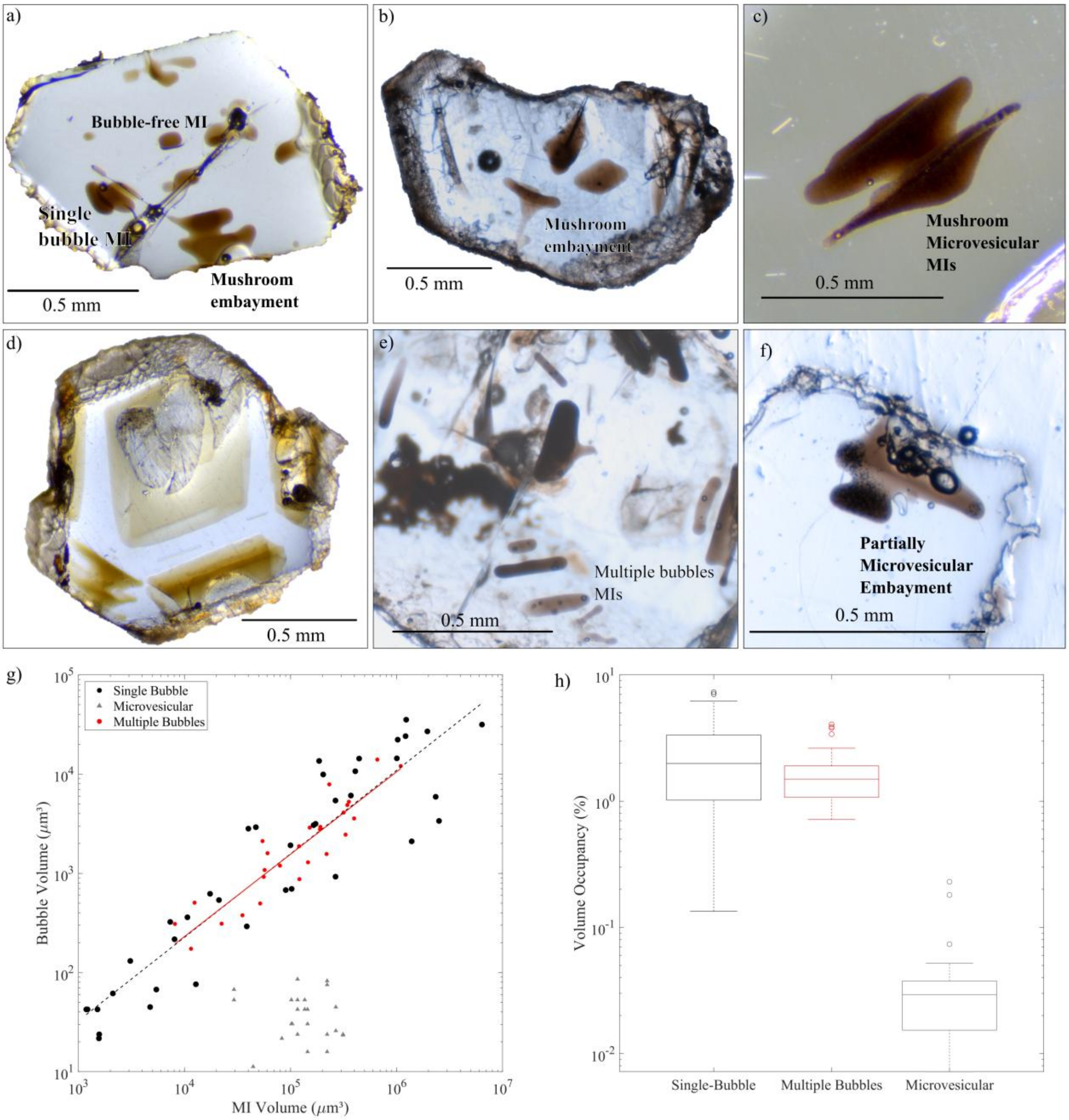

Fig. 5: Total alkali-silica diagram for the melt inclusions (including embayments), tephra matrix glass and pumice bulk rock compositions. The inset zooms in on the phonolite-trachyte field. *MI:* melt inclusions; *Tephra:* tephra glass matrix; *Bulk:* pumice whole rock.

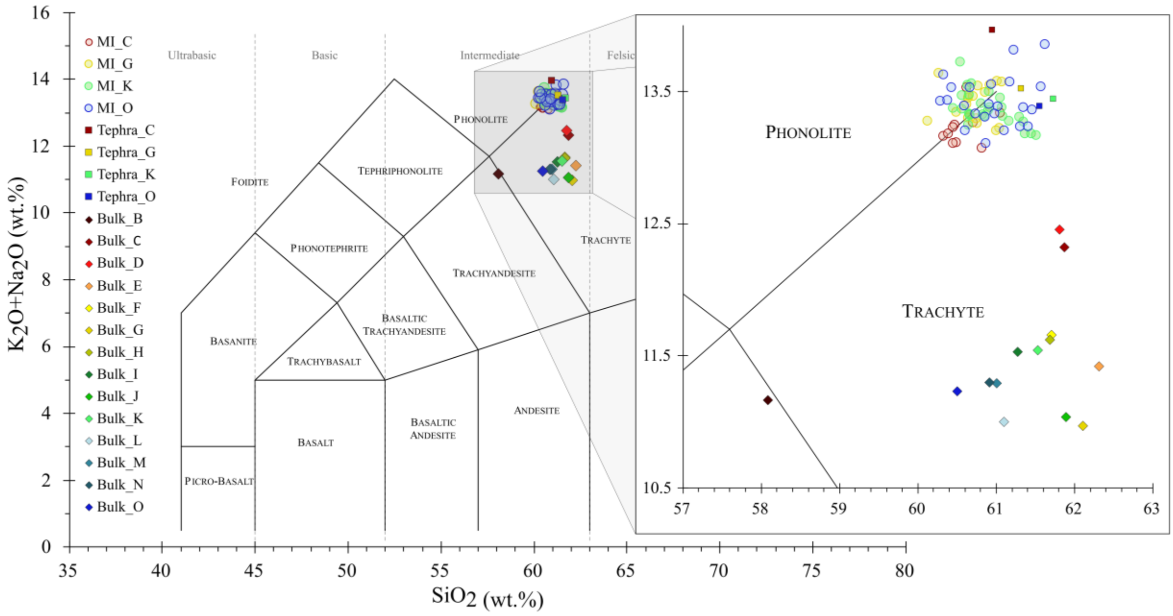

Fig. 6: Comparison of major element oxide concentrations of bulk rock, pumice matrix glass and haüyne-hosted melt inclusions. For reference, compositions of MIs hosted in various mineralogical phases after Fontijn et al. (2013) are also reported.

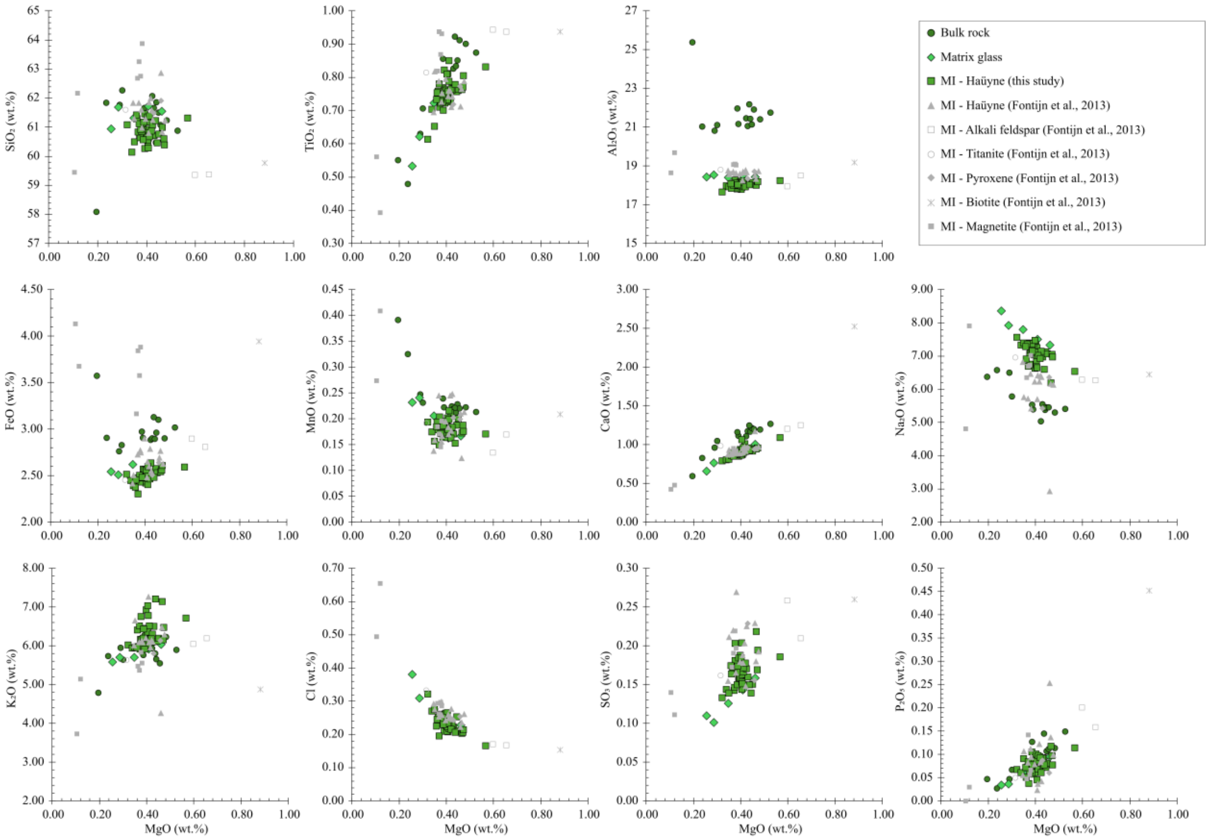

Fig. 7: **a)** and **b)** major element binary plots for melt inclusions and embayments; **c)** changes of major element concentrations across the deposit for melt inclusions, embayments and tephra matrix glass. The *red* and *blue* curves show mean values for each horizon for melt inclusions and embayments respectively.

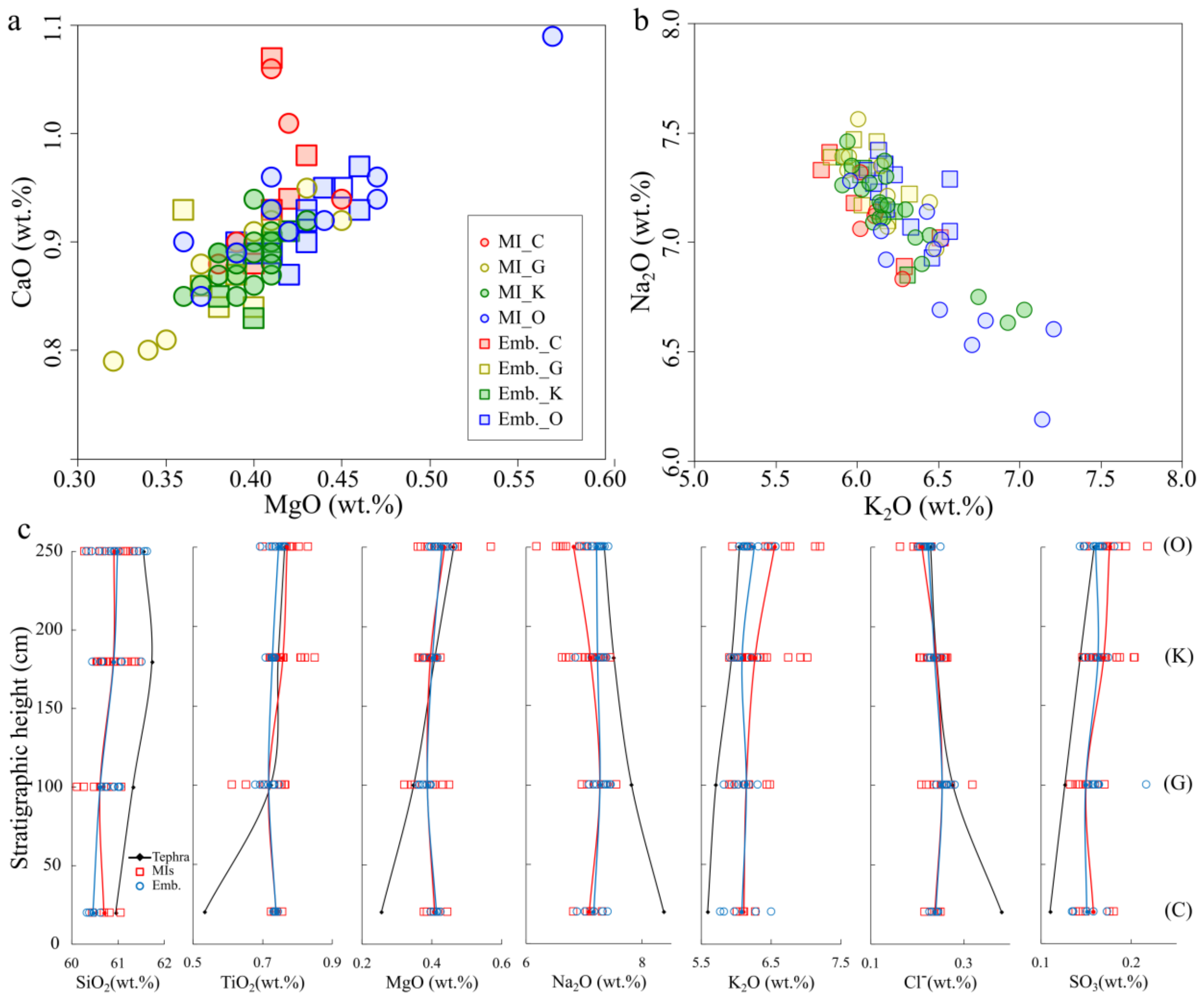

Fig. 8: *left axis*: Kernel density estimations of MIs and embayments water concentrations. The red dashed line indicates the uppermost quartile limit of H_2O distributions for MIs; *right axis:* Box-and-whisker plots of H_2O concentrations within MIs and embayments for the different horizons of the RP type section. The *inner line* indicates the median, w*hiskers* delimit the lower and upper quartiles, while *circles* indicate outliers.

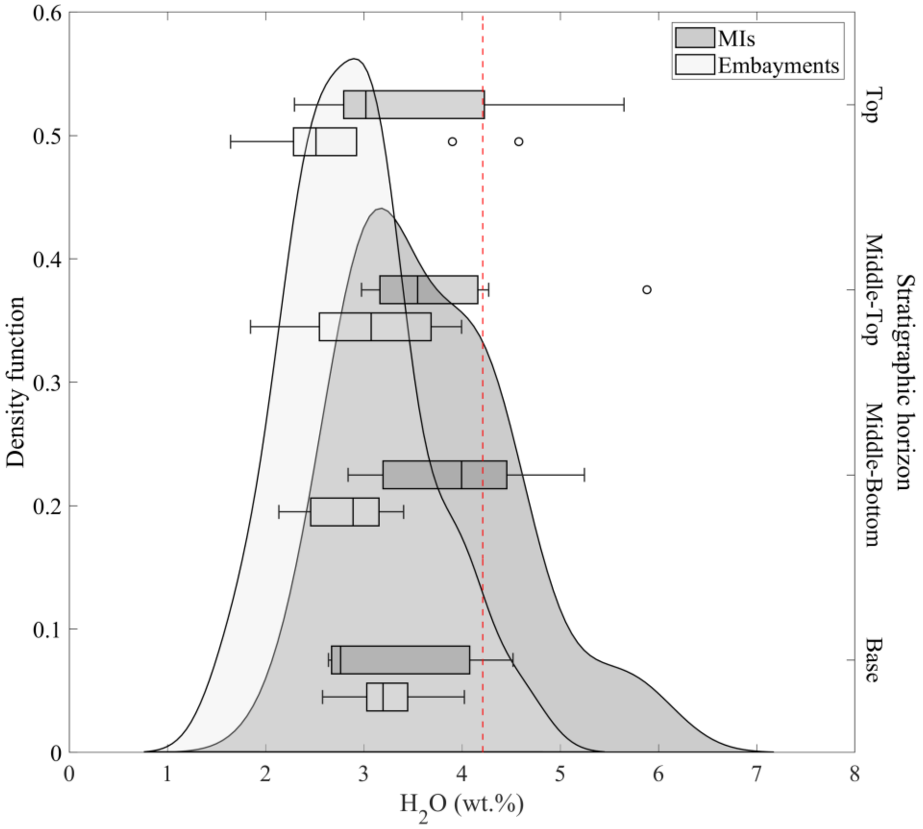

Fig. 9: a) Spider diagram of primitive mantle-normalised (McDonough and Sun, 1995) trace elements and **b)** REE for pumice bulk rock of the different stratigraphic horizons, compared to values available in the literature for RP pumice bulk rock (Fontijn et al., 2013) and for older Rungwe basalts (Castillo et al., 2014); **c)** comparison of the variation of concentration across the stratigraphic horizons for incompatible (i.e., increases from bottom to top of the magmatic reservoir; e.g., Zr) and compatible (i.e., decreases from bottom to top of the magmatic reservoir; e.g., Ba) trace elements. Hypothetical variations of element concentration as a function of fractional crystallisation (FC%) were computed assuming the horizon O as the less evolved (initial) liquid composition. Two cases were considered: the maximum (bulk partition coefficient, $D_{Zr} = 0$; *grey area*) and a lesser ($D_{Zr} = 0.3$; *yellow area*) incompatibility of Zr while the compatibility of Ba was ranged between $D_{Ba}=5$ and $D_{Ba}=25$. The bulk partition coefficient ranges were selected as the best areas enclosing data points after iterative attempts; **d)** comparison of the concentration variation across the stratigraphic horizons for two

incompatible elements. A hypothetical FC trend was traced assuming a total incompatibility (D = 0) for both elements. The legend shared by all diagrams is shown in panel **c)**.

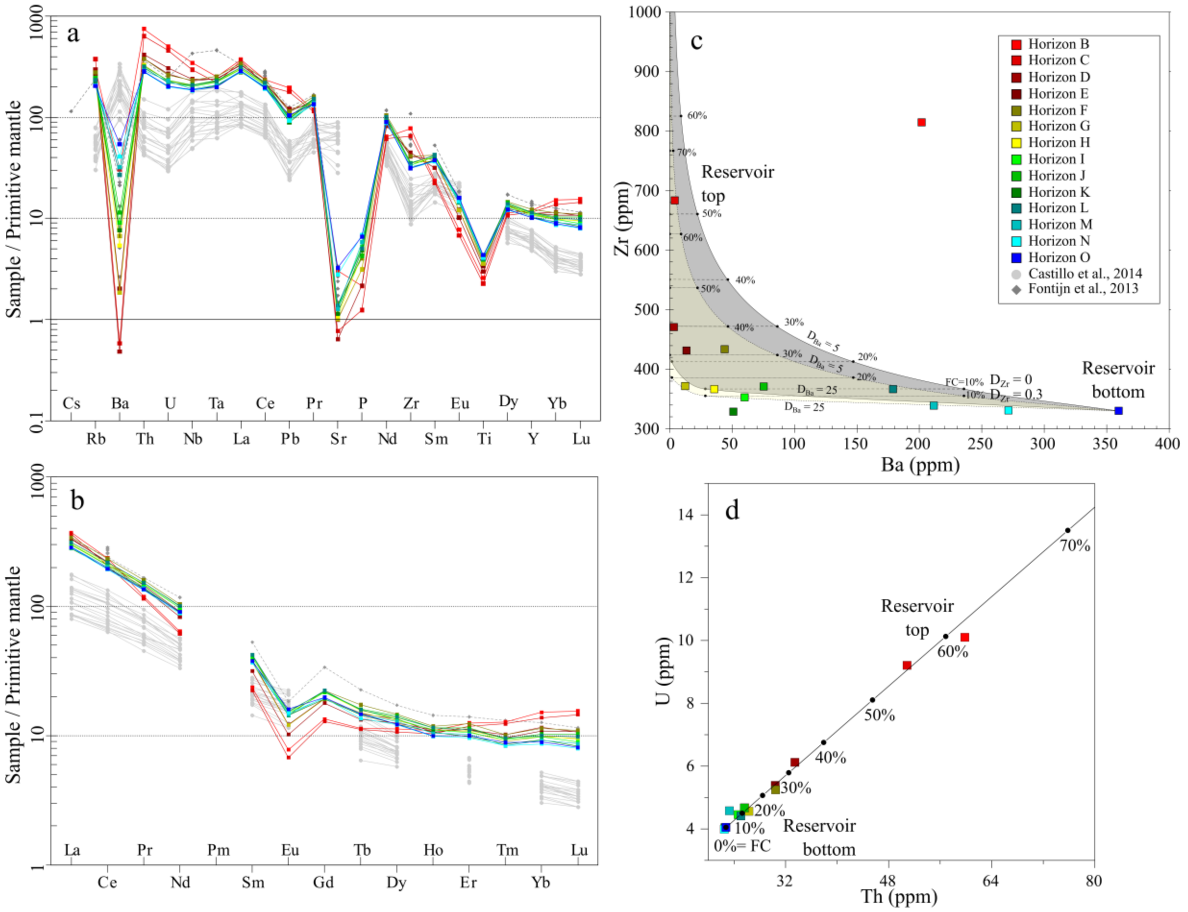

Fig. 10: **a**) Box-and-whisker plots of temperatures estimated for MIs using the alkali feldspar-liquid geothermometer (Putirka, 2008) across the stratigraphic sequence. The *inner line* represents the median, *whiskers* delimit the upper and lower quartiles and *circles* indicate outliers; **b)** *left axis*: Kernel density estimations of saturation pressures calculated using the Di Matteo et al. (2004) model. The red dashed line marks the lower pressure limit estimated from the upper quartile of H_2O distributions in MIs analyses; *right axis:* Box-and-whisker plots of saturation pressures across the RP type section. The *inner line* indicates the median, w*hiskers* delimit the lower and upper quartiles, while *circles* indicate outliers; **c)** comparison of Di Matteo et al. (2004) and MagmaSat solubility models. MagmaSat results including 90 ppm of CO_2 are

also shown. Error whiskers represent the 12% estimated uncertainty for water concentrations and the 12% uncertainty reported for the Di Matteo et al. (2004) model.

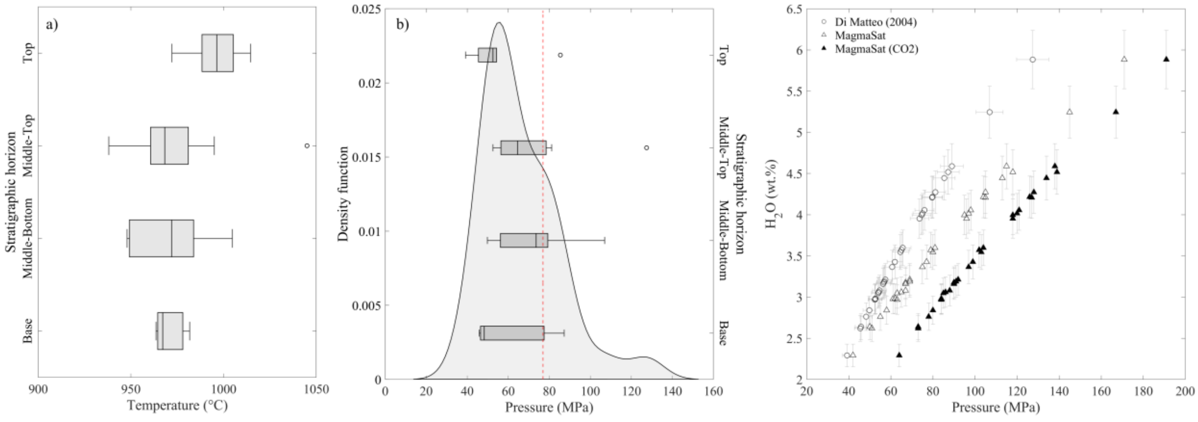

Fig.13: Schematic conceptual model of the proposed plumbing system dynamics preceding the Rungwe Pumice eruption. **a)** A magmatic batch evolves at depth from a presumably basaltic primitive magma forming a peralkaline trachytic melt. Early fractionation of biotite and pyroxenes occurs at a depth of up to 13 km (Fontijn et al., 2013); **b)** as magma ascends through the crust, alkali feldspars fractionation promotes the formation of a crystalline mush at the badse of the reservoir; **c)** gaseous phases sparging from depth induce haüyne crystallisation at shallow depths, likely destabilising the system and triggering the eruption. The role of a deep-rising magmatic plume remains uncertain. The eruption begins with a lower-intensity opening phase involving a shallower, older reservoir that underwent a distinct magmatic evolution; **d)** Eventually, prolonged gas sparging and/or magma input leads to the onset of a highly explosive eruption.

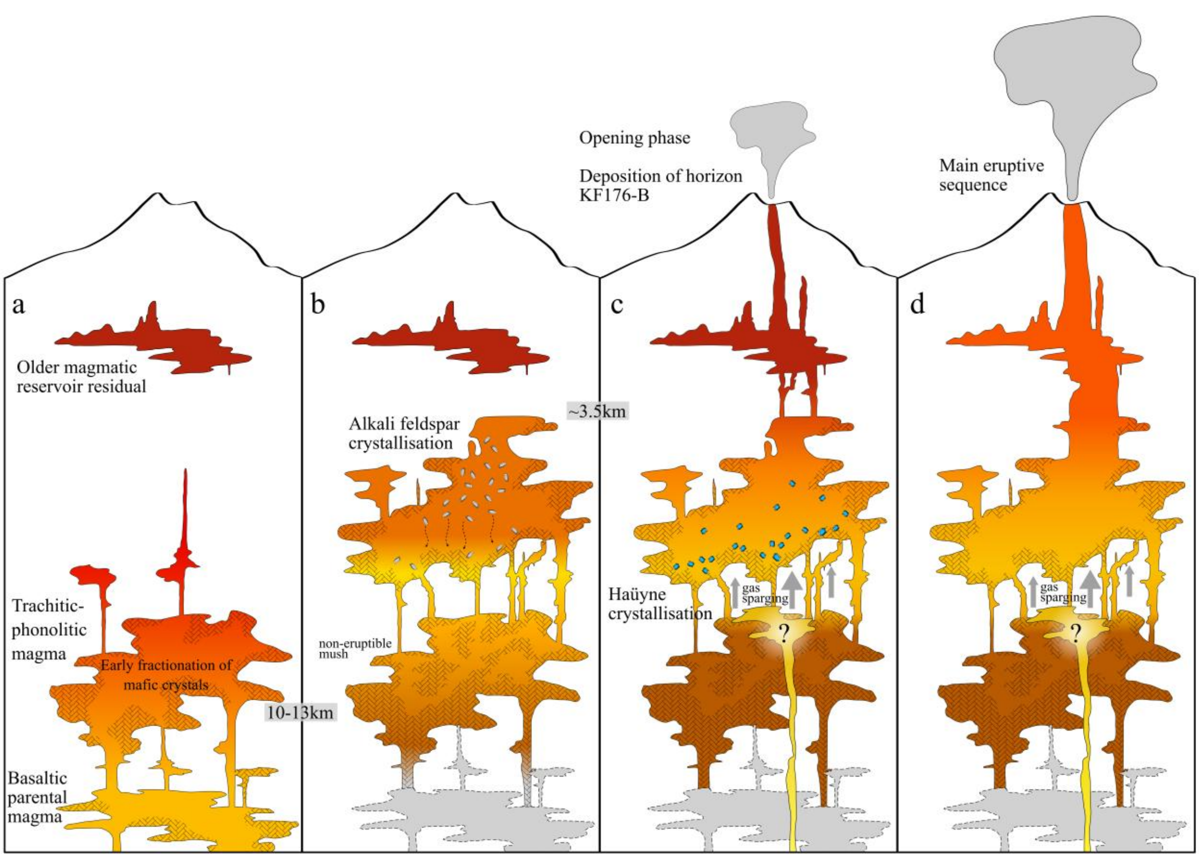
Opening phase
Deposition of horizon KF176-B
Main eruptive sequence
a
b
c
d
Older magmatic reservoir residual
Alkali feldspar crystallisation
~3.5km
Trachitic-phonolitic magma
Early fractionation of mafic crystals
10-13km
Basaltic parental magma
non-eruptible mush
Haüyne crystallisation
gas sparging
?
gas sparging
?

TABLES

Table 1
Major element compositions obtained with EPMA of pumice matrix glass of five different horizons of the Rungwe Pumice tephra deposit. Major and trace element composition of pumice bulk rock for the whole deposit were analysed with ICP-OES and Q-ICP-MS respectively. Bulk rock major element oxides are normalized to 100%.

Sample	Matrix glass					Bulk rock													
	KF176-C	KF176-D	KF176-G	KF176-K	KF176-O	KF176-B	KF176-C	KF176-D	KF176-E	KF176-F	KF176-G	KF176-H	KF176-I	KF176-J	KF176-K	KF176-L	KF176-M	KF176-N	KF176-O
wt.%																			
SiO_2	61.0	61.7	61.3	61.7	61.6	58.08	61.84	61.77	62.27	61.67	62.08	61.66	61.25	61.86	61.50	61.08	60.98	60.88	60.48
TiO_2	0.534	0.623	0.723	0.745	0.764	0.551	0.479	0.630	0.707	0.770	0.776	0.827	0.901	0.834	0.852	0.913	0.857	0.874	0.922
Al_2O_3	18.45	18.56	18.42	18.53	18.46	25.39	21.03	20.84	21.11	21.17	21.45	21.07	21.40	21.45	21.14	21.91	21.97	21.76	22.17
FeO	2.55	2.51	2.63	2.51	2.58	3.57	2.91	2.76	2.83	2.91	2.88	2.90	2.90	2.89	2.96	3.10	2.97	3.02	3.13
MnO	0.233	0.242	0.207	0.163	0.168	0.392	0.326	0.248	0.231	0.222	0.224	0.219	0.222	0.213	0.228	0.221	0.240	0.214	0.222
MgO	0.26	0.29	0.35	0.41	0.46	0.20	0.24	0.29	0.30	0.39	0.42	0.43	0.48	0.44	0.45	0.46	0.39	0.53	0.44
CaO	0.66	0.77	0.84	0.94	1.01	0.59	0.83	0.96	1.05	1.11	1.11	1.17	1.20	1.17	1.21	1.20	1.16	1.27	1.25
Na_2O	8.37	7.94	7.82	7.51	7.34	6.38	6.58	6.50	5.78	5.39	5.05	5.55	5.30	5.39	5.45	5.46	5.54	5.40	5.44
K_2O	5.59	5.71	5.71	5.93	6.05	4.80	5.74	5.96	5.65	6.27	5.94	6.08	6.24	5.66	6.10	5.56	5.76	5.90	5.81
Cl	0.382	0.310	0.277	0.242	0.229														
SO_3	0.11	0.10	0.13	0.14	0.16														
P_2O_5	0.035	0.037	0.061	0.085	0.096	0.05	0.03	0.05	0.07	0.09	0.07	0.09	0.11	0.09	0.11	0.11	0.13	0.15	0.14
Total	98.12	98.78	98.47	98.92	98.86	*norm.*	*norm.*	*norm.*	*norm.*	*norm.*	*norm.*	*norm.*	*norm.*	*norm.*	*norm.*	*norm.*	*norm.*	*norm.*	*norm.*
H_2O (b.d.)	1.88	1.22	1.53	1.08	1.14														
LOI						6.97	6.09	5.79	6.43	6.87	7.70	6.77	7.87	7.23	6.91	8.06	8.00	7.77	8.35
ppm																			
Sc						13.50	10.49	8.82	8.30	8.89	7.14	7.10	7.05	6.89	7.43	7.34	6.99	7.11	7.42
V						6.32	22.92	10.22	20.65	16.94	21.70	12.01	23.55	16.59	33.38	12.75	25.08	14.15	18.85
Cr						*bdl*	0.17	1.08	*bdl*	3.36	*bdl*	1.81	0.94	0.54	0.18	0.91	*bdl*	0.33	0.71
Co						0.33	0.15	0.26	0.19	0.65	0.29	0.30	0.69	0.40	0.59	0.65	0.37	0.68	0.58
Ni						*bdl*	*bdl*	*bdl*	*bdl*	*bdl*	*bdl*	*bdl*	*bdl*	*bdl*	*bdl*	*bdl*	*bdl*	*bdl*	*bdl*
Cu						15.33	9.11	29.80	8.60	10.94	5.41	8.98	9.29	9.24	5.03	7.52	4.90	5.52	4.24
Zn						175.71	115.40	100.73	79.74	86.25	68.83	104.11	74.57	79.63	81.91	79.25	73.83	71.48	70.45
Ga						57.03	49.20	51.30	50.22	53.68	47.38	48.66	49.71	50.58	47.14	51.37	46.82	46.95	47.63
Rb						179.08	225.89	177.70	163.26	166.19	145.02	145.69	141.47	148.61	133.17	140.89	123.87	124.83	122.65
Sr						60.79	15.25	12.65	19.92	28.27	20.05	21.41	26.79	25.77	22.64	27.42	25.29	55.25	64.64
Y						51.64	49.32	47.88	48.49	52.58	46.35	47.93	47.65	49.37	44.05	48.52	45.30	43.68	43.87
Zr						814.60	683.68	471.29	431.77	434.09	371.99	366.71	353.08	370.99	328.65	366.56	338.92	331.12	330.09
Nb						227.58	194.45	157.28	150.21	152.95	135.22	136.57	131.89	137.79	121.98	136.36	124.80	121.78	123.29
Ba						201.52	3.83	3.17	13.35	43.91	12.21	35.37	59.77	75.27	50.64	178.75	211.14	271.03	359.20
La						240.50	234.77	217.15	214.12	221.15	193.89	197.66	194.37	203.17	181.44	201.92	185.51	183.67	185.69
Ce						395.08	345.25	364.91	368.51	392.78	347.20	361.03	349.06	368.15	330.03	365.79	337.09	322.46	327.38
Pr						30.19	29.16	34.75	36.94	40.62	35.97	37.77	37.47	38.83	34.87	38.50	35.38	34.06	34.28
Nd						80.15	77.00	103.37	114.27	129.81	113.25	122.11	121.44	125.67	111.73	125.23	112.36	110.11	113.31
Sm						9.57	9.08	12.81	15.42	17.05	15.08	16.46	16.49	16.95	15.46	17.17	15.01	14.89	15.26
Eu						1.20	1.04	1.57	1.88	2.20	1.86	2.29	2.27	2.38	2.21	2.35	2.23	2.30	2.47
Gd						7.30	7.02	9.70	10.55	12.07	10.44	11.80	11.77	11.88	10.47	12.16	10.76	10.65	10.74
Tb						1.12	1.11	1.32	1.46	1.71	1.49	1.55	1.58	1.58	1.44	1.56	1.44	1.34	1.46
Dy						7.61	7.20	8.38	9.06	9.84	8.84	9.21	8.97	9.61	8.29	9.34	8.67	8.18	8.25
Ho						1.64	1.54	1.65	1.59	1.76	1.67	1.72	1.65	1.71	1.59	1.72	1.56	1.47	1.48
Er						5.49	5.16	4.83	4.96	5.41	4.69	4.78	4.60	5.01	4.31	4.82	4.49	4.20	4.37
Tm						0.87	0.84	0.69	0.66	0.69	0.61	0.65	0.64	0.64	0.59	0.65	0.57	0.57	0.60
Yb						6.69	6.05	5.10	4.77	5.02	4.33	4.39	4.30	4.55	4.08	4.42	4.05	3.80	3.93
Lu						1.06	0.99	0.72	0.73	0.75	0.65	0.64	0.61	0.70	0.56	0.67	0.59	0.54	0.55
Hf						15.16	13.10	9.41	8.59	8.71	7.55	7.36	7.19	7.58	6.51	7.43	6.79	6.41	6.46
Ta						9.35	8.09	8.84	8.93	9.38	8.42	8.53	8.27	8.61	7.58	8.45	7.70	7.39	7.37
Pb						29.29	26.79	18.09	17.03	17.21	14.69	14.90	14.37	15.17	13.43	14.49	14.01	13.96	15.71
Th						59.84	50.87	33.45	30.40	30.46	26.31	25.69	24.64	25.59	22.61	25.07	23.28	22.50	22.75
U						10.10	9.21	6.12	5.38	5.24	4.56	4.67	4.45	4.67	4.04	4.41	4.58	3.99	4.05

norm. = total major elements normalised to 100%; bdl = below detection limit.

Supplementary Information

a. **Supplementary Table 1:** Melt inclusions and embayment catalogue comprehensive of detailed descriptions of qualitative and quantitative features (available upon request to lorenzo.cappelli@ulb.be).
b. **Supplementary Table 2:** Chemistry data for melt inclusions, embayments, mineralogical phases and grey pumice glass. Results for the standards used as a reference for EPMA and mass spectrometry are also reported as well as the instrument conditions used for EPMA (available upon request to lorenzo.cappelli@ulb.be).
c. **Supplementary Table 3:** Results of thermobarometry models used to estimate the reservoir conditions. A summary of each barometry method used is reported together with the estimated storage depth for each (available upon request to lorenzo.cappelli@ulb.be).

d. Componentry Analyses:

Detailed methodology:

The different types of components that constitute the coarse ash portion of the Runge Pumice deposit were investigated for each subsample of the type section (KF176-B to KF176-O). The 0.355-0.500 mm (1.5φ-1φ) and the 0.710-1.000 mm (0.5φ-0φ) grain-size ranges were selected for the observations (hereafter termed medium and coarse ash fraction respectively). The fractions were partitioned up to six times using a sample splitter to reduce the sample size and still maintain a representative and functional amount. With the aid of a stereomicroscope, the clasts were characterised and allocated to 3 classes, i.e. juvenile, lithics and crystals (further subdivided into feldspars, mafic minerals, Fe-Ti oxides, haüyne and titanite), until a total of 3000 clasts per sample were categorised.

Results:

The coarse ash fraction of the deposit analysed is composed of three broad clast types: i) juvenile, ii) lithics, and iii) crystals. Juvenile clasts are cream-white highly vesicular pumices. Clast shapes are mostly solid, equidimensional and subrounded but, according to the size and shape of vesicles, can be more elongated or irregular. Lithic clasts include rock fragments of different nature extracted from the volcanic edifice, older lava deposits, and holocrystalline rocks. Free crystal phases include alkali feldspar, haüyne, pyroxene, biotite, Fe-Ti oxides, titanite, and accessory olivine. In the coarser ash fraction, the juvenile class is dominant in each layer of the deposit (always > 65% of the components), but it is substantially less dominant in the medium ash fraction (between 45% and 80% of the components) where the crystal content reaches up to the 45% of the components (**Fig. 1SI**). A gradual increase of the crystal content is observed from the bottom to the top of the stratigraphic section, particularly for the medium ash fraction, associated with an opposite trend of the juvenile content (**Fig. 1SI**). The lithic component represents a small fraction of both analysed grain sizes (3 - 12%) and it is almost constant along the stratigraphic section, except for a peak around 25 cm from the bottom (samples KF176C-KF176D) where it reaches up to 28% of the components (**Fig. 1SI**).

On average, 88% ± 3% and 96% ± 2% of the crystal component within the medium and coarse ash fractions respectively are represented by alkali feldspars (**Fig. 1SI**). Mafic minerals (pyroxenes and biotite) are the second most abundant crystalline component (between 3.4% and 10.5%) followed by Fe-Ti oxides (between 1.5% and 9.0%). Relative crystal abundances are almost constant throughout the stratigraphic column, apart from haüyne which shows a progressive increase from bottom to top, even though it never represents more than 3% of the crystal population (**Fig. 1SI**). The medium ash contains a smaller amount of haüyne, which is absent in the bottom 150 cm of the deposit (**Fig. 1SI**). Titanite crystals are found only in the medium ash and in small numbers (always < 0.9%).

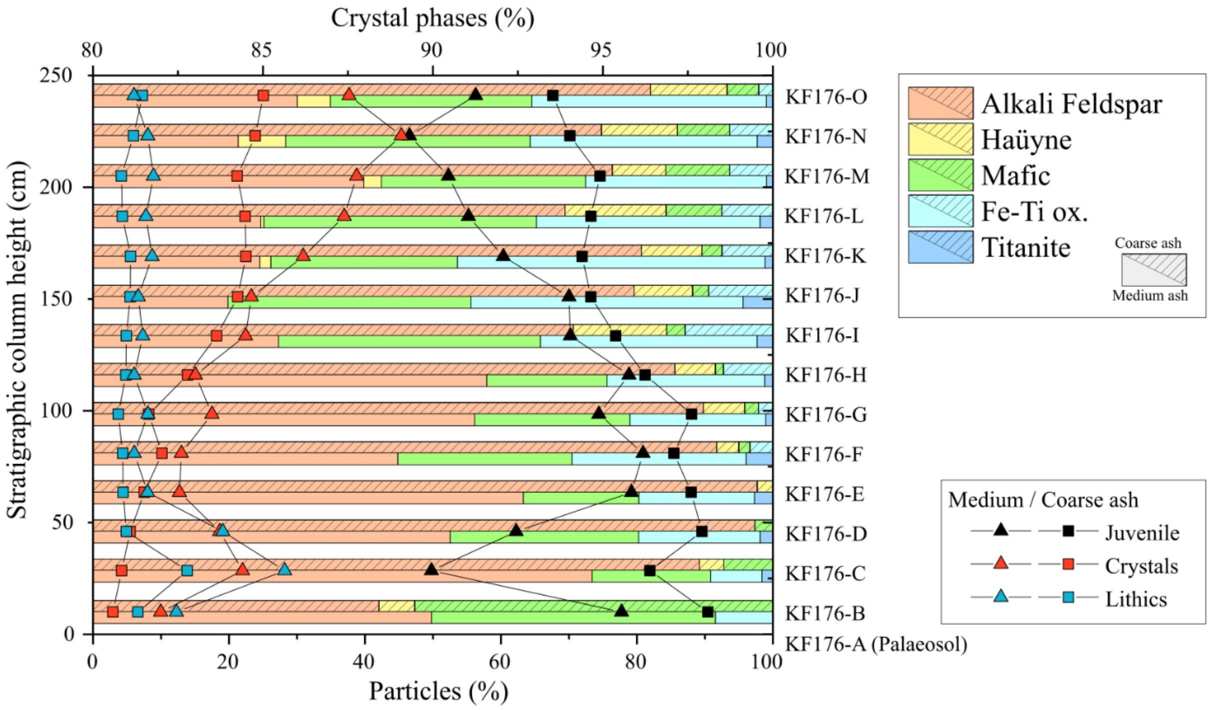

Supplementary Figure 1: Variations of componentry occurrence across the Rungwe Pumice deposit (*markers*). The top x-axis illustrates the cumulative distribution of the different crystalline phases (*bars*) within the crystal component. As the alkali feldspars always represent at least 80% of crystals, the axis origin was set at this value. For both, the medium and coarse ash grain sizes are reported separately.

e. MI water content analyses:

Detailed methodology:

To quantify the total amount of water dissolved within MI glasses we used the transmission Fourier Transformed Infrared spectroscopy technique (FTIR; §3.2.2). The FTIR method allows quantifying the sample absorbance for specific wavelengths in the near-/mid-infrared light range (usually between 1400 and 8000 cm^{-1}; von Aulock et al., 2014), which is caused by the vibration of specific molecules (analytes). The relationship between light absorption and the analyte concentration in the sample is described by the *Beer-Lambert Law,* which can be rewritten to express the analyte mass fraction (Stolper, 1982):

$$w = \frac{A \cdot M}{\epsilon \cdot l \cdot \rho} \times 100 \qquad (1)$$

where w is the analyte concentration in wt.%, A (dimensionless) the absorbance of the sample, corresponding to the height (or area) of specific peaks in the FTIR spectrum (§ 3.2.2), M the molecular weight of the analyte (e.g., 18.015 $g \cdot mol^{-1}$ for H_2O), ϵ ($l \cdot mol^{-1} \cdot cm^{-1}$) the composition-dependant absorptivity index of the sample for the analyte of interest, l (cm) the thickness of the sample crossed by the beam, and ρ the density of the sample (in $g \cdot l^{-1}$).

Sample preparation

Alkali feldspar crystals in the RP deposit host MIs and embayments (i.e., inclusions open on one side), however, their lamellar shapes and tiny volumes made them impractical to be used for this study. MIs hosted in pyroxenes and Fe-Ti oxides were hard to identify due to the dark and opaque colour of the crystals. Haüyne crystals instead tend to contain visibly more MIs than the other mineral phases and therefore represented the best target for this investigation. Five stratigraphic horizons representative of the bottom (KF176-C), middle (KF176-G and KF176-K), and top (KF176-O) sequences of the deposit type section were selected. For each layer, several pumice clasts in the 11.3-16 mm (-3.5φ/-4φ) grain-size range were manually crushed. Over 100 haüyne crystals were handpicked from the crushed material in the 0.5-2 mm (1φ/-1φ) grain-size range and subjected to careful observation and sample selection. The crystals were placed on a glass slide and embedded in a thermosetting resin (Crystalbond™ 509). An exploratory first polishing of the crystal surfaces allowed a detailed description of MI features and recognition of potential melt inclusion assemblages (MIAs, i.e., groups of coeval MIs originated from the same magma at the same reservoir conditions; Bodnar and Student, 2006; Esposito et al., 2014) which helps in describing the history of both the MI and MI's host.

Moreover, FTIR measurements require a clear path large enough to let the infrared beam pass through the sample to avoid any contamination of the spectrum. Therefore, small MIs (i.e., smaller than 15 µm, the minimum infrared beam aperture) or MIs hosting too many bubbles were discarded (§ 4.2).

To ensure that only the MI was crossed by the infrared beam, the crystals hosting MIs or embayments suitable for analyses were polished on two sides in a way that two parallel surfaces of the selected MIs were exposed (doubly exposed; von Aulock et al., 2014). Firstly, the crystals were grounded on one side with a 6 µm diamond paste until one or more MIs were properly exposed. Final polishing was achieved with progressively finer-grade diamond pastes (3 µm and 1 µm). Finally, the crystal was gently removed from the resin and flipped over to expose and polish the opposite side of the MI following the same process. This way we obtained fragile crystal wafers tens of micrometres thick. Eventually, a variable number of MIs per layer was successfully prepared because of crystal availability and MIs' suitability for analyses, for a total of 86 MIs and embayments.

Infrared absorption

The transmission FTIR spectra of MIs were acquired at the ISTO-CNRS laboratory (Orleans, France) using a Nicolet 6700 FTIR spectrometer connected to a Nicolet Continuµm Infrared Microscope equipped with a MCT IR Detector Module. The acquiring setup consisted of a Globar light source, an XT-KBr beamsplitter and a 32x infinity-corrected Schwarzschild objective matching to a 32x condenser. The crystals were gently removed from the resin after heating on a hot plate, then rinsed in acetone to remove any resin residuals and placed over a CaF_2 window.

The fundamental stretching vibration of O-H bonds in H_2O and OH^- absorbs infrared light at the 3550 cm^{-1} wavenumber (**Fig. 2**). The height (or area) of this characteristic overtone peak in

IR spectra is directly proportional to the total concentration of water in the sample, and usually, it retains a good signal-to-noise ratio. However, this overtone can be easily saturated at relatively high water concentrations unless the thickness of the sample is extremely thin (von Aulock et al., 2014). In that case, water concentration can be measured by the combination of the absorbance band of the hydroxyl group (OH^-; 4500 cm^{-1}) with the band of molecular water (5200 cm^{-1}). Therefore, we acquired spectra in the 1200-6000 cm^{-1} wavenumbers unit range with a spectral resolution of 4 cm^{-1} (**Fig. 2**). The aperture of the square beam was set at 20x20 µm or 40x40 µm when the size of the MI allowed it, while a 15x15 µm beam aperture was exceptionally used for the smallest MIs. For each spectrum, 256 (512 for the 15x15 µm beam aperture) acquisitions were collected. A background spectrum on the CaF_2 window was collected for calibration before each sample analysis, and every time the spectra showed abnormal trends due to environmental changes in temperature, CO_2 concentration or humidity. We chose to use peak heights instead of areas as they are less subjected to peak distortions, especially for the combination bands. Finally, we adopted a linear baseline to measure peak intensity. A minimum of three scans were collected for each melt inclusion for reproducibility which were then averaged through the data processing tools of Omnic™ software to reduce the spectral noise. FTIR spectra were acquired at the centre of MIs but also closer to rims to evaluate the consistency of the estimated water content, while embayments were scanned in their most internal portions.

The molar absorptivity index in Eq. (1) is a composition-dependent constant that can be determined for each glass composition once the water content is constrained with other analytical methods (e.g., Karl Fisher titration or secondary ion mass spectrometry). However, absorptivity indices present in the literature for glasses with a chemical composition similar to that of the sample can be applied with good approximation (von Aulock et al., 2014). For high-alkali trachytic glasses a value of 66.9 ± 5.8 $l \cdot mol^{-1} \cdot cm^{-1}$ was experimentally determined for the 3550 cm^{-1} overtone (Behrens and Hahn, 2009) while absorptivity indices for the 4500 cm^{-1} and 5200 cm^{-1} overtones (ϵ_{4500} and ϵ_{5200}) were estimated through a multiple linear regression based on the absorbance values of the 4500 cm^{-1} and 5200 cm^{-1} peaks (A_{4500} and A_{5200} respectively), according to the following relationship (Di Matteo et al., 2004):

$$\frac{w_{3550}}{100} = \frac{1}{\epsilon_{4500}} \cdot \frac{A_{4500}M}{l\rho} + \frac{1}{\epsilon_{5200}} \frac{A_{5200}M}{l\rho} \qquad (2)$$

where w_{3550} is the water content (in wt.%) calculated with the 3550 cm^{-1} band and used as a fixed term for the regression. The regression was performed including those spectra that did not reach saturation and at the same time showed well-shaped combination bands. It was iteratively reproduced by systematically excluding those spectra values that deranged the interpolation until a satisfying goodness was achieved ($r^2 \approx 0.9$). The regressed molar absorptivity indices and their 90% confidence bounds (subscript and superscript values) measured $1.35_{1.01}^{1.71}$ l·mol^{-1}·cm^{-1} and $1.03_{0.69}^{1.38}$ l·mol^{-1}·cm^{-1} for the 4500 cm^{-1} and 5200 cm^{-1} overtones respectively. These indices are similar but slightly different from those previously estimated for trachytic (1.58 l·mol^{-1}·cm^{-1} and 1.36 l·mol^{-1}·cm^{-1} respectively; Di Matteo et al., 2004) and phonolitic (1.25 l·mol^{-1}·cm^{-1} and 1.10 l·mol^{-1}·cm^{-1} respectively; Carroll and Blank, 1997) glass.

Thickness

The MI thickness is a fundamental parameter that must be carefully determined as it represents one of the major sources of error in Eq. (1), especially for the thinner crystal wafers. For example, in our dataset, a difference of 1 μm produces on average a ~3% percentage error on the water content estimation, equivalent to 0.1 wt.% H_2O. Moreover, during sample preparation, it is important to monitor the thickness of the samples as this could determine which absorbance band can be used (von Aulock et al., 2014). To minimise the uncertainty introduced by operator's biases (e.g., optical focus recognition) two different methods were applied, and the results compared. Firstly, the thickness was measured with a flat-anvil digital micrometre (resolution = 1 μm; accuracy = ±2 μm). A flat micrometre was chosen over a pointed micrometre to minimise the risk of damaging or disrupting the extremely fragile crystals. Once we ensured that crystals were adhering properly to their glass slides, each glass slide was measured together with the hosted crystal and on its own. Crystal thickness was then obtained by difference. The measurements were repeated two or three times per crystal. Subsequently, we used an optical microscope with calibrated focus stages. A LEITZ DMR microscope equipped with an automated stage (resolution = 2 μm) was used, and each crystal was measured two times for consistency.

To verify the consistency of the thickness measurements, we applied the spectral fringes counting method for those transmission spectra that showed interference fringe patterns (Nichols and Wysoczanski, 2007; von Aulock et al., 2014). This method consists of counting the spectral fringes in a specific spectral region where no absorption peaks are present (usually in the 2000-2700 cm^{-1} range; Wysoczanski and Tani, 2006), and which relate to the thickness (l) following the equation (Nichols and Wysoczanski, 2007):

$$l = \frac{m}{2n(v_1 - v_2)} \qquad (3)$$

where m is the number of waves, n is the refractive index of the sample (dimensionless), and v_1 and v_2 are the highest and lowest wavenumber (in cm^{-1}) respectively of the selected spectral interval. Interference fringes were detected on both haüyne crystals and MIs, and refractive indices of 1.50 and 1.52 were used respectively (Taylor, 1967; Keller et al., 1978). While a good correlation was found between thicknesses measured with the optical focus stages method and the digital micrometre, a systematic underestimation (35.4% ± 18% percentage error on average) was observed between the results obtained with these methods and the thicknesses estimated by the interference fringes method.

Glass density

The density of MI glass has been estimated as a function of its chemical composition at room temperature following the equation (Lange, 1997):

$$\rho_{298K} = \frac{\sum X_i \, M_i}{V_{298K}} \tag{4}$$

where X_i represents the mole fraction of each major oxide component (i), and M_i their molecular weights. The volume of the glass at room temperature (V_{298K}) is considered equivalent to the volume of the glass at the quenching temperature (V_{liq}) as no contraction after solidification is expected because of the volume-constrained nature of MIs and the fast cooling in the atmosphere of pumiceous tephra. Therefore, the contribution of the thermal expansion coefficient (Eq. (4) in Lange, 1997) was not considered and the glass volume at quenching temperature was estimated using the equation for iron-bearing silicate glasses, modified after Lange and Carmichael (1987):

$$V_{liq}(T) = \sum X_i \,(T) V_i(T) + X_{Na_2O} X_{TiO_2} V_{Na_2O-TiO_2} + X_{H_2O} V_{H_2O}(T) \tag{5}$$

where V_i is the volume regression of major oxide components as a function of the liquid temperature with respect to the volume at the modelled temperature of 1300 °C (Lange and Carmichael, 1987):

$$V_i(T) = V_{i,1573K} + \frac{dV_i}{dT}(T - 1573K) \tag{6}$$

and $V_{H_2O}(T)$ is the temperature-dependent molar volume of water modelled starting from the volume at ~1000 °C (Ochs III and Lange, 1999; Richet et al., 2000). The mole fractions of the MI's major oxides (X_i) were derived from chemical analyses measured with a JEOL JX-iHP200F field emission electron probe micro-analyser (EPMA) at the IMAP laboratories of the Université Grenoble-Alpes (France). The crystal wafers were embedded in epoxy resin, polished (down to 1 µm diamond grade), and carbon coated. We used an acceleration voltage of 15 kV, a probe current of 5 nA, and a defocused beam diameter of 15 µm to analyse the MIs.

The analytes were measured with four WDS (wavelength dispersive spectroscopy) and one EDS (energy dispersive spectroscopy; Si only, with StHs6-80 glass as calibration material) spectrometers. Sodium was analysed first to avoid element dispersion and a ZAF correction was applied. The StHs6-80, Atho-G and KE12 reference materials (Jochum et al., 2006) were analysed three times each, after every 30-40 measurements to evaluate accuracy. Each MI was measured at least three times for consistency. Water concentrations were roughly estimated using the by-difference method (e.g., Devine et al., 1995).

To constrain the MI's temperature *T,* equivalent to the fictive temperature of the pre-eruption silicate liquid, we applied the alkali feldspar-liquid geothermometer (Eq. (24b) in Putirka, 2008). This thermometer describes the chemical equilibrium between magmatic melts and alkali feldspars as a function of temperature. Alkali feldspar crystals were handpicked from the 0.5-2 mm grain-size fraction of crushed pumices and then embedded in epoxy resin. Pumiceous glass shards were obtained from the 125-250 μm grain-size fraction of manually crushed pumice clasts. The crushed material was rinsed and wet sieved at 80 μm in demineralised water to remove accretionary dust or clays and embedded in epoxy resin. Grain mounts of glass shards and alkali feldspar crystals were grounded and polished with diamond paste down to a grade of 1 μm. Alkali feldspar composition was analysed by EPMA, using the same instrument and analytical conditions as those used to analyse the haüyne-hosted MIs, and with Cr-Augite, Ortho-Bl3 and Ortho-Bl2 as secondary standards. For the glass shards, a 2 nA probe current and a 5 μm beam diameter were used. We analysed glass from each layer at least eight times for reproducibility, while core-to-rim transects of 5 measurements were performed on the alkali feldspars. As the alkali feldspar-liquid geothermometer does not foresee an equilibrium constant to constrain the equilibrium between melt and alkali feldspars (Putirka, 2008), to assess equilibrium between feldspar rims and pumice groundmass, petrographic observations of thin sections from five stratigraphic subsamples (KF176B; KF176E; KF176H; KF176K; KF176N) were conducted using optical petrographic microscopy and scanning electron microscopy (SEM). SEM imaging was performed in backscattered electron mode, at 15 kV using a Hirox SH5500P equipped with a Bruker EDS Quantax detector at the Laboratoire G-Time of the Université libre de Bruxelles (Belgium). No disequilibrium features were identified. However, before applying feldspar-based thermometry, textures of feldspars analysed with EPMA were further assessed via SEM. Haüyne density was assumed to be 2.4 $g \cdot cm^{-3}$ (Taylor, 1967).

f. Principal component analysis

A principal component analysis of MI major element concentrations allowed to identify the most relevant oxides affecting the chemical variability of the melt, in an attempt to identify chemically differentiated magmas co-occurring in the magmatic reservoir. The three most representative principal components were used to identify chemically distinct clusters of MIs through hierarchical clustering.

Results:

The principal component analysis of MI glass composition suggests that the chemical variance is dominated by K_2O, Na_2O and SiO_2, which constitute the majority of the first three principal components and represent a total variance of ~26%, ~25% and ~23% respectively. The attempt to cluster the MIs according to their stratigraphic horizon was unsuccessful. Instead, the first three principal components, which represent ~96% of the variance, were used to group the data into two major chemical clusters plus an outlier sample (**Fig. 2SI**) through a hierarchical clustering. While the first cluster includes only six MIs, the second cluster includes most of the MI dataset and represents a slightly more silicic magma, enriched in Na_2O and depleted in K_2O (**Fig. 2SI**). The incorporation of MIs in one or the other cluster is not related to the distribution within crystals or to whether it hosts a shrinkage bubble. However, all the MIs belonging to the more evolved first cluster are found in the topmost stratigraphic horizons.

Supplementary Figure 2: Principal component analysis of major element concentrations: for each melt inclusion (including embayments) the values of the three major principal components obtained are shown together with the variance contribution of each element (blue lines). The samples were divided into two major clusters (green and cyan ellipses) plus an outlier (red dot) through hierarchical clustering. Statistical distribution of SiO2, Na2O, K2O and H2O concentrations for each cluster are shown in violin plots.

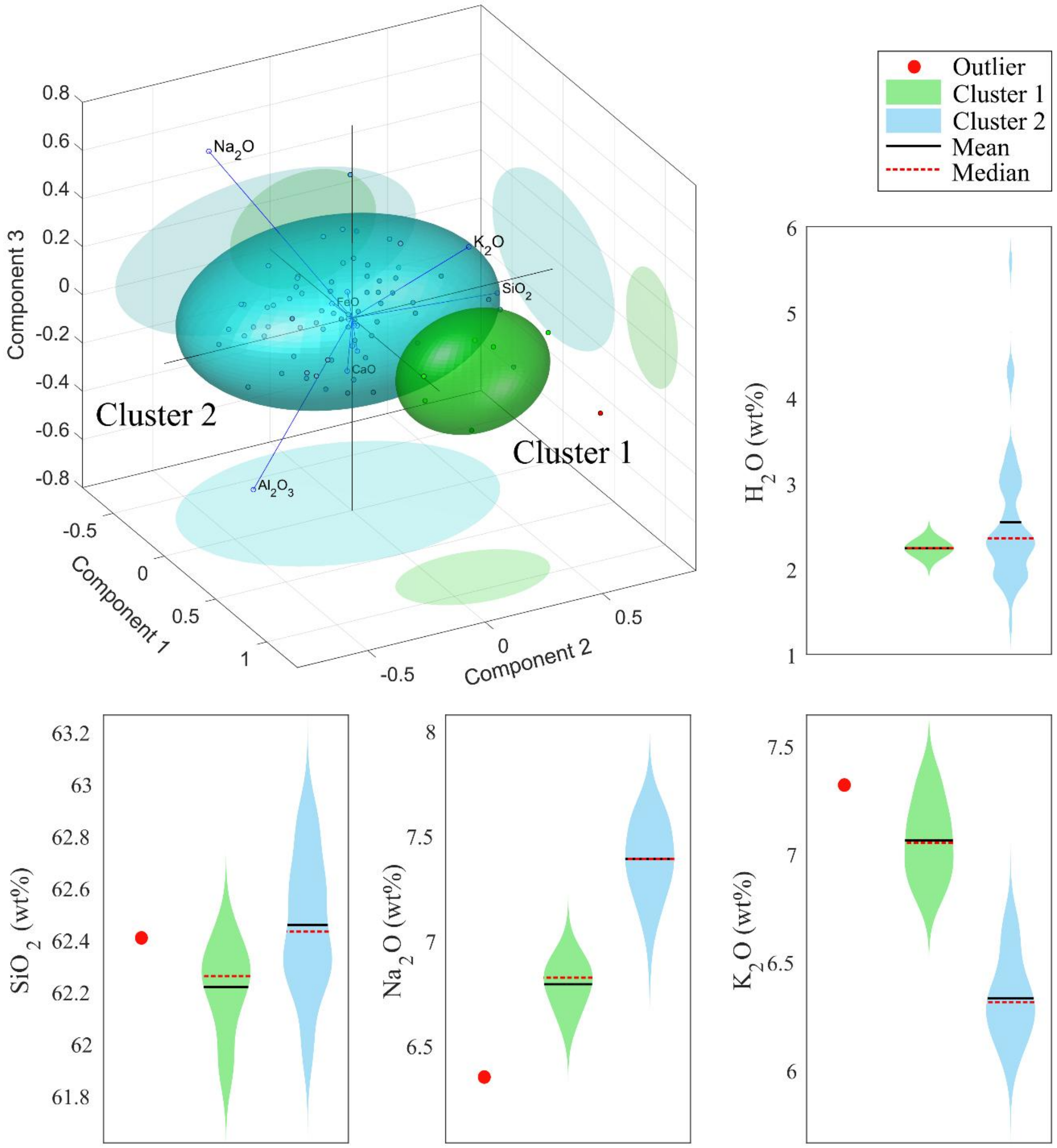

g. **Supplementary Figure 3SI:** Backscattered electron images of haüyne crystals showing zeolitic alterations tens to hundreds µm thick around crystal surfaces; b) The energy dispersive X-ray spectroscopy (EDS) mapping of relative chemical concentrations shows in false colours the enrichment in Al and Ca in the zeolite and the depletion of sulfur. Mn veins are also present. Images were collected with an accelerating voltage of 15 kV using a Hirox SH5500P scanning electronic microscope (SEM) equipped with a Bruker EDS Quantax detector at the Laboratoire G-Time of the Université libre de Bruxelles (Belgium).

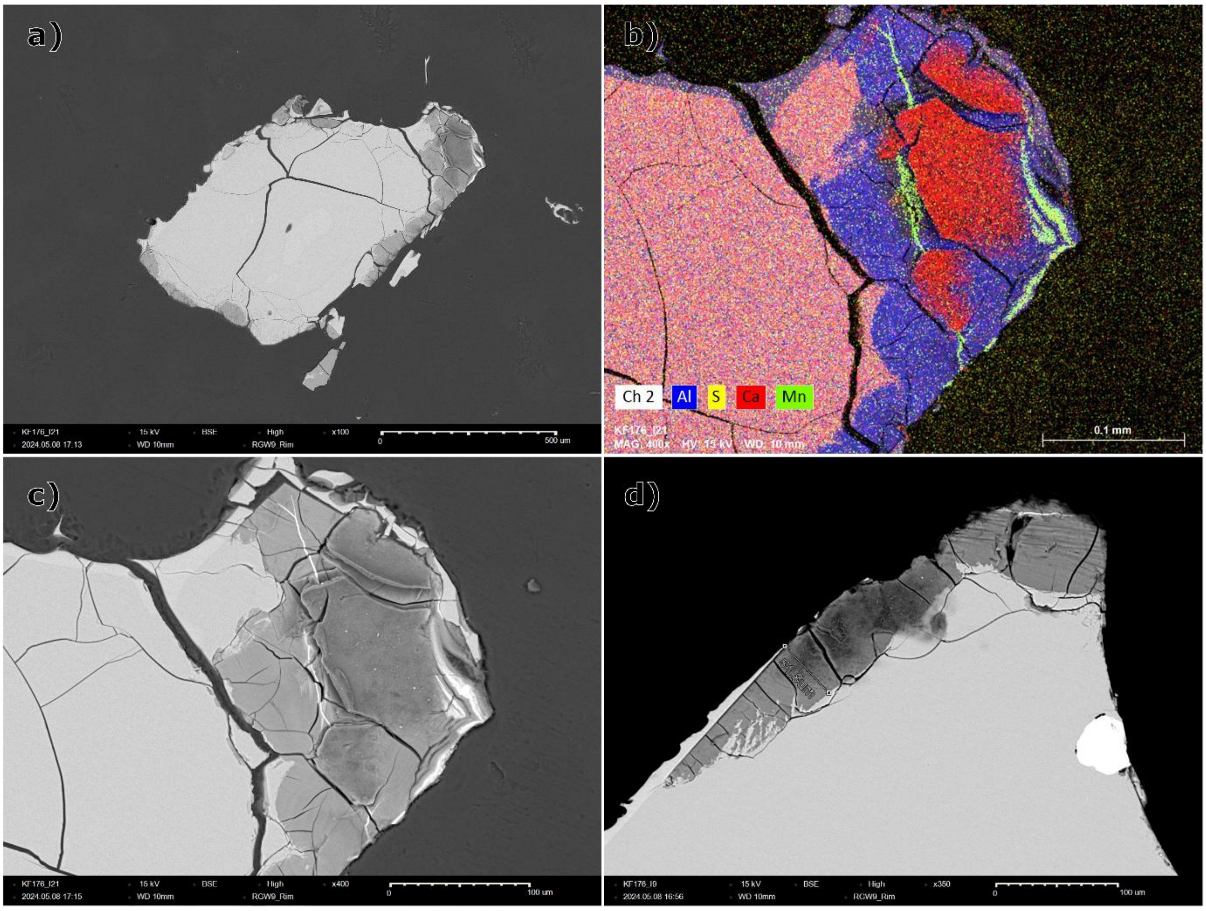
a)
KF176_I21
2024.05.08 17.13
15 kV
WD 10mm
BSE
High
RGW9_Rim
x100
0
500 um
b)
Ch 2
Al
S
Ca
Mn
KF176_I21
MAG: 400x HV: 15 kV WD: 10 mm
0.1 mm
c)
KF176_I21
2024.05.08 17:15
15 kV
WD 10mm
BSE
High
RGW9_Rim
x400
0
100 um
d)
KF176_I9
2024.05.08 16:56
15 kV
WD 10mm
BSE
High
RGW9_Rim
x350
0
100 um

a. **Supplementary Figure 4: a)** Feldspar ternary diagram reporting core and rim analyses of alkali feldspars. Phyton3 tool Thermobar (v.0.07; Wieser et al., 2022) was used for data plotting; **b)** SEM backscattered electron image of an alkali feldspar crystal showing no evident textural zonation. The *red line* indicates the core-to-rim transect of analyses. (*Wieser, P.E., Petrelli, M., Lubbers, J., Wieser, E., Özaydın, S., Kent, A.J.R., Till, C.B., 2022. Thermobar: An open-source Python3 tool for thermobarometry and hygrometry. Volcanica 5, 349–384. https://doi.org/10.30909/vol.05.02.349384*).

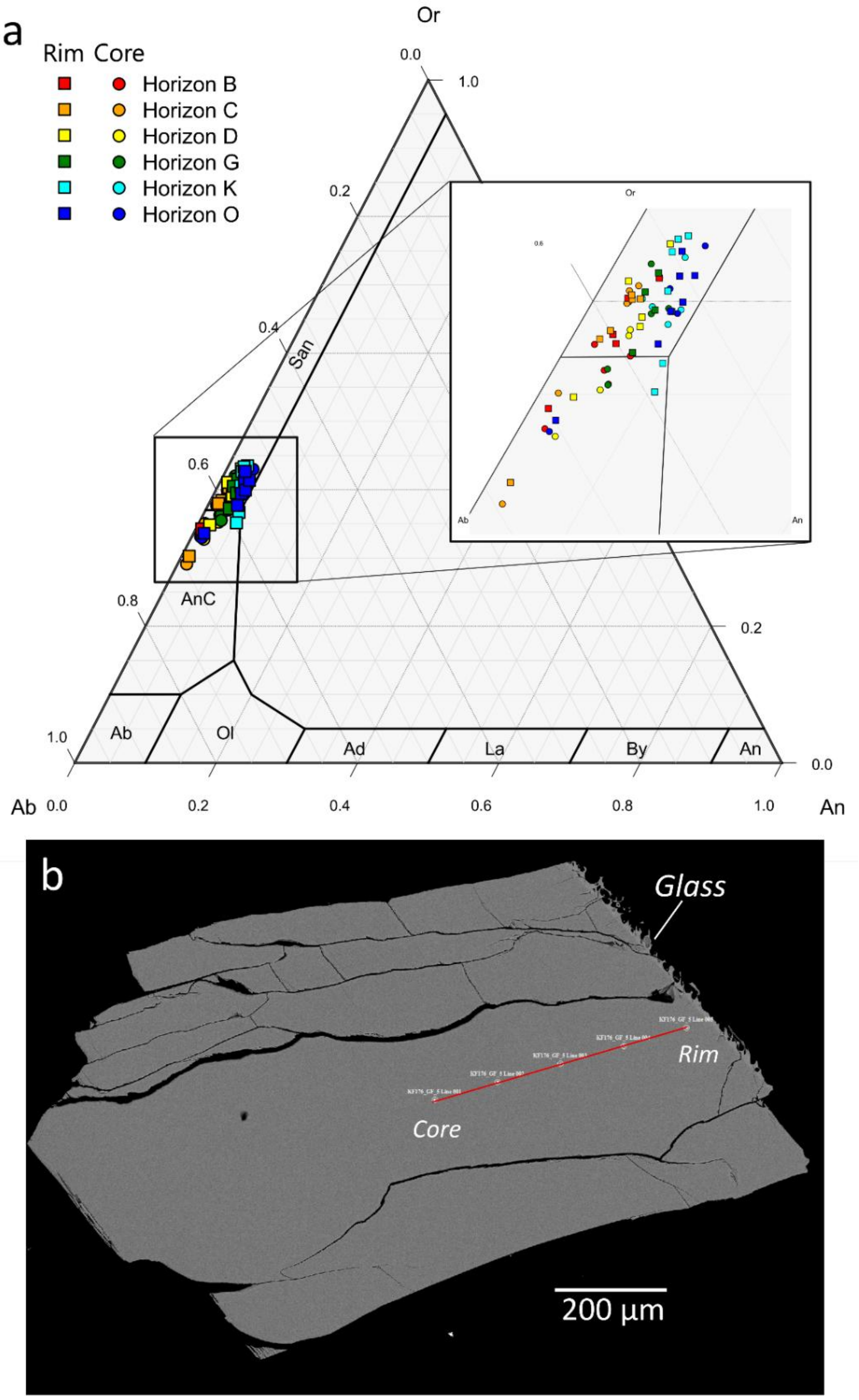
a
Or
Rim Core
Horizon B
Horizon C
Horizon D
Horizon G
Horizon K
Horizon O
0.0
1.0
0.2
0.4
0.6
0.8
San
AnC
Ab
Ol
Ad
La
By
An
Or
0.6
Ab
An
Ab 0.0
0.2
0.4
0.6
0.8
1.0 An
b
Glass
KF176_GF_5 Line 005
KF176_GF_5 Line 004
KF176_GF_5 Line 003
KF176_GF_5 Line 002
KF176_GF_5 Line 001
Rim
Core
200 µm